Cell Reports

Article

Exploring the longitudinal glioma microenvironment landscape uncovers reprogrammed pro-tumorigenic neutrophils in the bone marrow

Graphical abstract

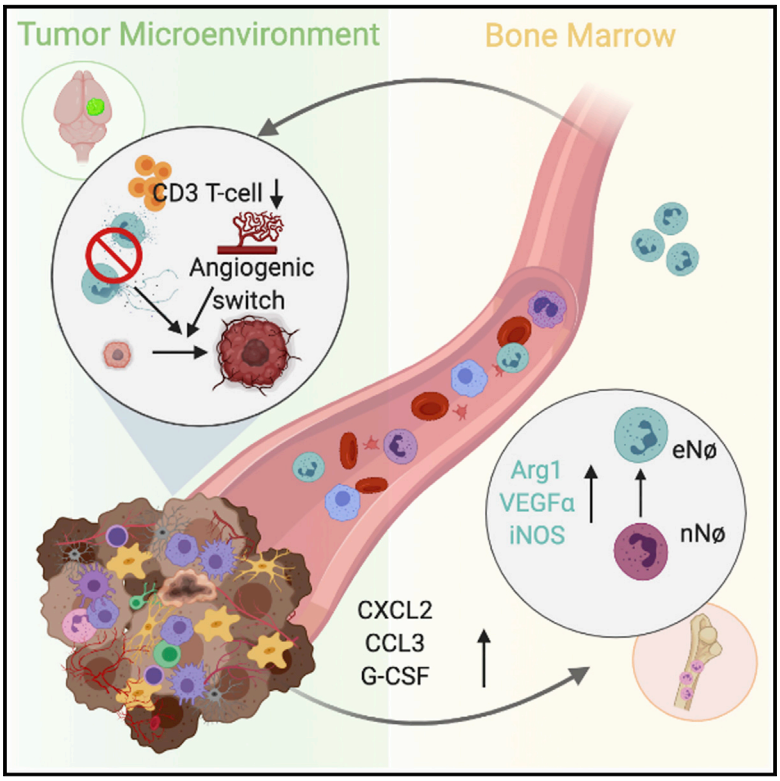

Authors

Prerna Magod, Ignacio Mastandrea, Liat Rousso-Noori, Lilach Agemy, Guy Shapira, Noam Shomron, Dinorah Friedmann-Morvinski

Correspondence

dino@tauex.tau.ac.il

In brief

Magod et al. reveal immature neutrophils with pro-tumorigenic properties in the bone marrow of glioblastoma-bearing mice. These findings provide evidence of systemic reprogramming of bone marrow neutrophils and the effect of early polarization in brain tumor progression.

Highlights

- R53-induced gliomas present higher recruitment of peripheral immune cells
- Neutrophils levels are higher from initiation through progression in R53 tumors
- Depletion of neutrophils at initiation stage facilitates tumor growth
- Bone marrow-derived neutrophils switch from anti- to pro-tumorigenic phenotype

Magod et al., 2021, Cell Reports *36*, 109480
August 3, 2021 © 2021 The Author(s).
https://doi.org/10.1016/j.celrep.2021.109480

CellPress

Cell Reports

CellPress
OPEN ACCESS

Article

Exploring the longitudinal glioma microenvironment landscape uncovers reprogrammed pro-tumorigenic neutrophils in the bone marrow

Prerna Magod,[1] Ignacio Mastandrea,[1] Liat Rousso-Noori,[1] Lilach Agemy,[2] Guy Shapira,[3] Noam Shomron,[3] and Dinorah Friedmann-Morvinski[1,4,5,6,*]

[1]The School of Neurobiology, Biochemistry and Biophysics, The George S. Wise Faculty of Life Sciences, Tel Aviv University, Tel Aviv 6997801, Israel
[2]Department of Plant and Environmental Sciences, Weizmann Institute of Science, Rehovot, Israel
[3]Sackler Faculty of Medicine, Tel Aviv University, Tel Aviv 6997801, Israel
[4]Sagol School of Neuroscience, Tel Aviv University, Tel Aviv, Israel
[5]Twitter: @DfmLab
[6]Lead contact
*Correspondence: dino@tauex.tau.ac.il
https://doi.org/10.1016/j.celrep.2021.109480

SUMMARY

Recent multi-omics studies show different immune tumor microenvironment (TME) compositions in glioblastoma (GBM). However, temporal comprehensive knowledge of the TME from initiation of the disease remains sparse. We use Cre recombinase (Cre)-inducible lentiviral murine GBM models to compare the cellular evolution of the immune TME in tumors initiated from different oncogenic drivers. We show that neutrophils infiltrate early during tumor progression primarily in the mesenchymal GBM model. Depleting neutrophils *in vivo* at the onset of disease accelerates tumor growth and reduces the median overall survival time of mice. We show that, as a tumor progresses, bone marrow-derived neutrophils are skewed toward a phenotype associated with pro-tumorigenic processes. Our findings suggest that GBM can remotely regulate systemic myeloid differentiation in the bone marrow to generate neutrophils pre-committed to a tumor-supportive phenotype. This work reveals plasticity in the systemic immune host microenvironment, suggesting an additional point of intervention in GBM treatment.

INTRODUCTION

Malignant high-grade gliomas are associated with disproportionately high morbidity and mortality. These cancers exhibit relentless malignant behavior characterized by widespread invasion throughout the brain, resistance to traditional and newer targeted therapeutic approaches, destruction of normal brain tissue, and certain death. The median age of individuals at the time of diagnosis is 64 years. Despite harsh treatment and improving standards of care, the median survival is only 12–15 months for individuals with glioblastoma (Furnari et al., 2007). Unresponsiveness may result, at least in part, because these therapies only aim to target cancer cells and neglect the complex microenvironment around tumors that undergo drastic changes during disease development.

The Cancer Genome Atlas (TCGA) originally classified glioblastoma into four molecular distinct subtypes: neural, proneural (PN), classical (CL), and mesenchymal (MES) (Verhaak et al., 2010). In the past few years and as a result of more robust gene expression analyses, only three subtypes—PN, MES, and CL—are recognized, with the PN and MES subtypes having more reproducible signatures among different studies. In glioblastoma, recent reports clearly show that inter-tumor heterogeneity, first associated with tumor-intrinsic transcriptional heterogeneity, is accompanied by changes in the immune microenvironment (Friebel et al., 2020; Kaffes et al., 2019; Klemm et al., 2020; Martinez-Lage et al., 2019; Wang et al., 2017). In some of these studies, the changes in the immune microenvironment were analyzed by single-cell transcriptomic analysis (single-cell RNA sequencing [scRNA-seq]) from resected tumors before and after therapeutic intervention as well as flow cytometry and immunohistochemistry in bulk tumors. In addition, a second layer of heterogeneity associated with the developmental state of intratumoral glioma cells has been reported recently and suggested to be influenced by the tumor microenvironment (Neftel et al., 2019).

Using a lentiviral Cre-inducible mouse model of glioblastoma (GBM), we have shown previously that gliomas can be initiated from differentiated cells in the central nervous system (CNS), including cortical neurons (Friedmann-Morvinski et al., 2012). Using this model, we showed that transduction of neural stem cells (NSCs), astrocytes, or even mature neurons can give rise to malignant gliomas and proposed glioma cell plasticity as an alternative source to generate intratumor heterogeneity

This is an open access article under the CC BY-NC-ND license (http://creativecommons.org/licenses/by-nc-nd/4.0/).

(Friedmann-Morvinski and Verma, 2014). In the present study, we aimed to elucidate the longitudinal microenvironment changes from tumors initiated from different oncogenic drivers, HRas-shp53 (R53) and PDGFB-shp53 (PD53), associated with the human MES and PN GBM molecular subtypes, respectively. Flow cytometry analysis of lentivirally induced GBM tumors at three different time points—initiation, progression, and endpoint—revealed significant fluctuations primarily in the myeloid compartment. We find that tumor-associated macrophages (TAMs), defined by a mixture of activated brain-resident microglia and infiltrating bone marrow-derived macrophages (Gabrusiewicz et al., 2016; Hambardzumyan et al., 2016) indeed constituted the majority of the infiltrating immune cell population, in agreement with previous reports. In this study, we report that neutrophils constitute a dynamic myeloid subpopulation and reveal its different roles and effects on GBM.

Neutrophils have been historically recognized as the first responders in pathogenic infections (Borregaard, 2010). Today, in addition to their primary function in host defense, neutrophils play critical roles in bridging innate and adaptive immune responses, regulating hematopoiesis, angiogenesis, and wound repair (Granot, 2019). In the context of cancer, neutrophils have been shown to infiltrate the microenvironment in several types of tumors, and in recent years, there has been increasing interest in understanding how neutrophil infiltration can affect tumor progression. In terms of nomenclature, neutrophils and monocytes with immunosuppressive activity are called myeloid-derived suppressor cells (MDSCs). MDSCs can be divided into two subpopulations: granulocyte (g) or polymorphonuclear (PMN) MDSCs and monocytic (m) MDSCs. In mice, neutrophils and PMN MDSCs are morphologically and phenotypically similar and can only be distinguished functionally based on their ability to suppress other immune cells (Veglia et al., 2021).

Here we show that neutrophils preferentially infiltrate R53-induced tumors that closely resemble human MES GBM. Moreover, neutrophil infiltration commences at early tumor phases and is maintained throughout tumor progression. *In vivo* depletion of neutrophils at tumor initiation revealed that the early-infiltrating neutrophils reduced tumor growth—a capacity that is lost as tumor progresses. As opposed to tumor-associated neutrophils (TANs)/PMN MDSC, which have been mostly studied, we show here that bone marrow-derived neutrophils from R53 tumor-bearing mice are pre-committed to a pro-tumorigenic functional phenotype. Our results reveal that functional regulation of neutrophils occurs earlier than known previously, in the bone marrow, and is influenced by oncogenic drivers, uncovering a tumor-bone marrow (BM) signaling pathway influencing neutrophils. Hence, understanding how BM-resident neutrophils are programmed by the tumor to adopt a cancer-promoting phenotype may be used as an additional and potential therapeutic approach to inhibit GBM.

RESULTS

Generation and characterization of murine GBM models induced by different oncogenic drivers

We have previously used Cre-inducible lentiviral vectors to generate murine glioma models that closely recapitulate the histopathological characteristics observed in human disease (Marumoto et al., 2009). We next expanded application of this lentiviral system and included two hits in the same viral construct (e.g., HRasV12 expression and p53 inactivation) and showed that gliomas can originate from differentiated cells (e.g., neurons) or undifferentiated NSCs/progenitor cells (Friedmann-Morvinski et al., 2012). We injected the same oncogenic lentiviral vector (R53) into the cortex (CTX) of SynapsinI-Cre (SynI-Cre) host mice to induce GBM and named this model R53 (Figure 1A; Figure S1A). We have reported previously that tumors derived from SynI-Cre mice injected in the CTX with R53 exhibit a very strong MES molecular subtype signature characterized by elevated *Acta2*, *Chl3l1* and fibronectin (Figures 1B and 1C; Figure S1B; Angel et al., 2020; Friedmann-Morvinski et al., 2016). Taking advantage of our flexible lentiviral system and using a different oncogenic driver, we generated a second model representing the human PN GBM subtype. We injected glial fibrillary acidic protein (GFAP)-Cre mice in the subventricular zone (SVZ) with a lentivirus expressing PDGFB and shp53 (named PD53). RNA-seq analysis of PD53-induced tumors confirmed expression of the PN molecular signature (Figure 1B), and qPCR results validated expression of the PN markers *DLL3*, *Olig2*, and *NCAM2* (Figure S1B). Confocal microscopy analysis showed expression of Olig2 and lack of the mesenchymal marker fibronectin (Figure 1C). Importantly, the median overall survival of the mouse models follows the same trend observed in the human PN and MES subtypes, with a relatively favorable outcome for PD53-initiated tumors compared with R53 tumors (Figure 1D; Verhaak et al., 2010).

Driver mutations differentially shape the immune cell microenvironment

Gene expression signatures have been shown previously to be associated with inflammation and altered immunological landscapes. This variation in immune cell composition results from secretion of different cytokines and chemokines, which may stimulate infiltration of distinct immune cell subpopulations (Amankulor et al., 2017; Martinez-Lage et al., 2019; Wang et al., 2017). To evaluate whether the genetic driver mutations associated with human GBM molecular subtypes differentially shape the immune microenvironment, we performed flow cytometry analysis (fluorescence-activated cell sorting [FACS]) of tumors derived from the models generated and described above (Figure 1). Mice were injected with the oncogenic (experimental) or mock (control group) lentivirus, and tumors were collected at the endpoint. The tumors were first dissociated into a single-cell suspension, and the overall $CD45^+$ immune population was compared (Figure S2A). As shown in Figure 2A, PD53 tumors have significantly more overall $CD45^+$ immune cells than R53 tumors. Next, to identify the immune cell repertoire in the tumor microenvironment, we enriched for the $CD45^+$ population in all tumors and analyzed the different immune subsets (Figures S2A and S2B). We first looked at the myeloid compartment and overall expression of the CD45 and CD11b markers. Historically, these two markers were used to distinguish between resident microglia ($CD11b^+CD45^{low}$) from peripheral monocyte-derived macrophages ($CD11b^+CD45^{high}$) (Sedgwick et al., 1991). However, this strategy has been challenged in recent years, opening new discussions regarding the composition of

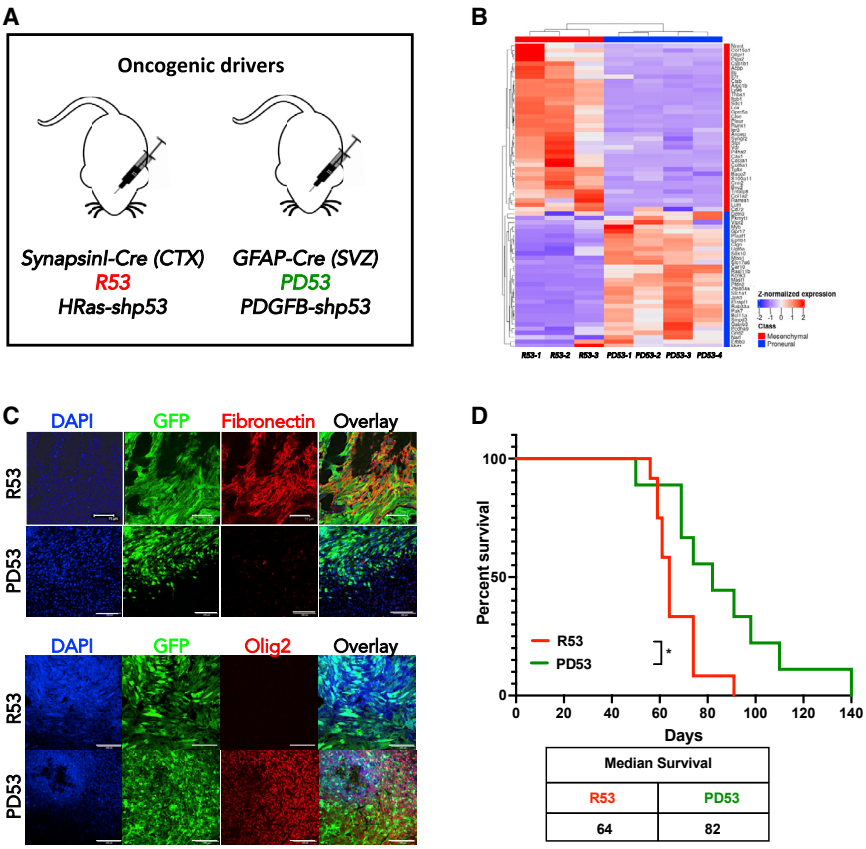

Figure 1. Generation and characterization of murine GBM models by injection of Cre-inducible oncogenic lentiviral vectors

(A) Graphical scheme summarizing the oncogenic driver combinations, transgenic mice, and stereotaxic sites of injection used to generate the murine GBM models.

(B) Heatmap of RNA-seq analysis by gene expression subtypes (Wang et al., 2017) in representative lentivirally induced murine R53 and PD53 tumors (n = 3–4).

(C) Representative immunofluorescence images of R53 and PD53 tumor sections stained with fibronectin and Olig2 markers of MES and PN tumors, respectively. DAPI was used as nuclear marker, and GFP is expressed only in tumor cells. Scale bars, 75 μm (only in the topmost panel) and 100 μm.

(D) Kaplan-Meier survival curves showing overall survival of R53 versus PD53 lentivirally induced tumors (n = 10). Median overall survival for each GBM model is summarized in the table below the curves.

Log rank test was used to calculate p values. * $p < 0.05$. See also Figure S1 for a lentiviral vector diagram and qRT-PCR analysis of R53 and PD53 tumors.

the myeloid cell compartment in gliomas (Charles et al., 2011; Glass and Synowitz, 2014; Hambardzumyan et al., 2016). In rodent glioma models, these two different myeloid cell populations have been identified, with $CD11b^{+}CD45^{high}$ cells demonstrated to include macrophages as well as microglia (Brandenburg et al., 2017; Müller et al., 2015). Interestingly, analysis of these two populations revealed that R53-initiated tumors have significantly more $CD11b^{+}CD45^{high}$ cells than PD53-initiated tumors (Figure 2B). Further analysis of the $CD11b^{+}CD45^{high}$ myeloid population (see gating strategy in Figure S2B) confirmed that these differences were extended to macrophages, mMDSCs, and neutrophils (Figure 2B). The FACS results were validated for some of these populations by confocal microscopy analysis, showing infiltration of microglia, macrophages, and neutrophils in the tumor area compared with adjacent brain tissue (Figure S2C).

The percentage of $CD3^{+}$ T cells varied slightly between the different oncogenic driver models. Analysis of T cells revealed that $CD4^{+}$ T cells dominated in R53 tumors, whereas $CD8^{+}$ cells were most abundant in PD53 tumors (Figures 2C and 2D).

Altogether, our analysis revealed that although R53-initiated tumors have overall fewer $CD45^{+}$ cells, they present higher recruitment of peripheral immune cells ($CD11b^{+}CD45^{high}$; Figures 2A and 2B). These results confirmed previous and recent findings suggesting that the human MES molecular subtype is associated with inflammatory infiltrates (Kaffes et al., 2019; Martinez-Lage et al., 2019; Wang et al., 2017).

Fewer immune cells infiltrate in PD53 tumors following chemotherapy treatment

A subpopulation of cells in the tumor with stem-like properties, usually called glioma stem cells (GSCs), have been held responsible for glioma formation, maintenance, and invasiveness, and, most importantly, extensive studies have implicated these GSCs in tumor recurrence (Lathia et al., 2015). GSCs can be subdivided into two main groups, MES or PN, based on their molecular signatures (Marziali et al., 2016). In experimental GBM models, this divergence is reflected by responsiveness to therapy, with the MES signature being mostly therapy resistant and the PN subtype mostly therapy responsive (Fedele et al., 2019). To investigate whether therapeutic response associated with GBM molecular subtypes influences immune cell infiltrates, we isolated tumor-derived GSCs from our R53 and PD53 lentivirally induced murine models, hereafter called R53-GSCs and PD53-GSCs, respectively. After confirming their molecular subtype (Figure S2D), we transplanted these GSCs into the brain of immunocompetent syngeneic mice to determine the differences in the immune cell infiltration following temozolomide (TMZ) chemotherapy treatment, given by oral gavage for 10 days. In the first experiment, we showed that, although R53-GSC model is resistant to TMZ treatment, the PD53-GSC model is more sensitive to the drug (Figure S2E). In the second experiment, when untreated mice reached the endpoint, all mice were euthanized, and immune cell infiltration was analyzed by flow cytometry. Although no changes were observed in the more resistant R53-GSC model, significant depletion of immune cell infiltration was observed in TMZ-treated PD53-GSC tumors (Figures 2E and 2F), suggesting that sensitivity to the drug in PD53-induced

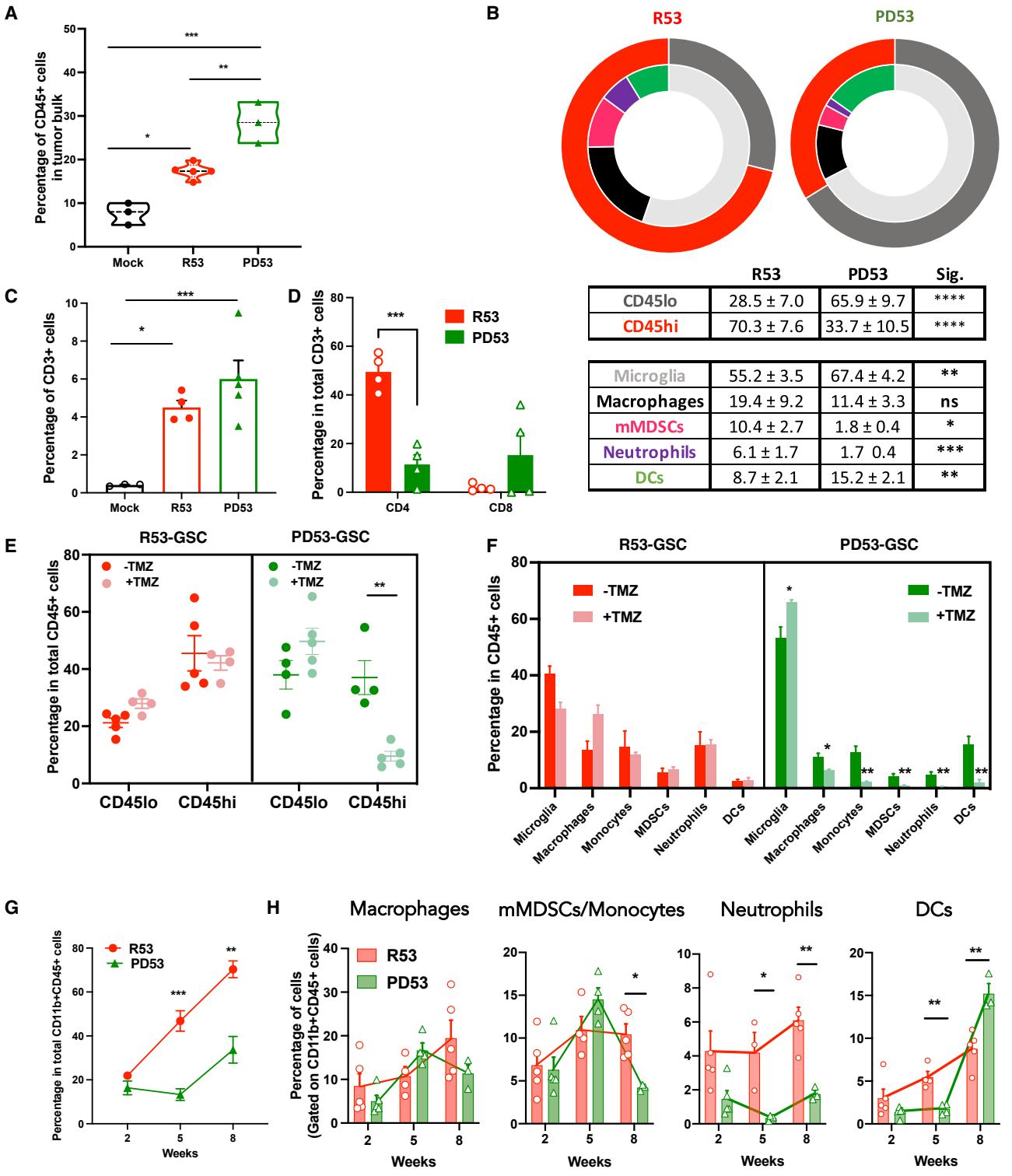

	R53	PD53	Sig.
CD45lo	28.5 ± 7.0	65.9 ± 9.7	****
CD45hi	70.3 ± 7.6	33.7 ± 10.5	****

Microglia	55.2 ± 3.5	67.4 ± 4.2	**
Macrophages	19.4 ± 9.2	11.4 ± 3.3	ns
mMDSCs	10.4 ± 2.7	1.8 ± 0.4	*
Neutrophils	6.1 ± 1.7	1.7 0.4	***
DCs	8.7 ± 2.1	15.2 ± 2.1	**

Figure 2. Immune cell characterization in different GBM mouse models

(A) Graph showing CD45$^+$ cells in the tumor bulk.

(B) Flow cytometry analysis of CD11b$^+$CD45^{lo} and CD11b$^+$CD45^{hi} cells from the indicated tumors; quantification of each subpopulation, considering CD11b$^+$CD45$^+$ as 100%, is indicated in the table (see gating strategy in Figure S2B). Results are presented as mean percentage ± SEM.

(C) FACS analysis of CD3$^+$ cells (gated on live cells) from the indicated tumors compared with mock-injected control mice.

(legend continued on next page)

tumors modeling human PN GBM (Figure S2E) affects the immune cells infiltrating the tumor microenvironment as a function of the tumor origin.

Differences in immune cell profile are observed early during GBM progression

The cellular arm of the tumor microenvironment is a heterogeneous subset of non-transformed cells that provides nutrients and various factors, influencing the development and progression of the tumor. Changes in overall abundance and distribution of myeloid cell subpopulations at different time points along tumor development may therefore provide insight into how immune cells of the TME affect tumor growth dynamics. For this, we took advantage of our lentivirally induced murine GBM models to follow the cellular changes that occur from initiation through progression of the disease. Based on the average latency of these tumors, we performed FACS analysis 2, 5, and 8 weeks after lentiviral tumor induction. We observed a steady increase in the population of infiltrating myeloid cells ($CD11b^{+}CD45^{high}$) in R53-induced tumors compared with PD53-induced tumors, reaching the peak near the end-point (8 weeks) (Figure 2G). Next we performed a longitudinal analysis of the subpopulations in this compartment. Although there were fluctuations between the different tumors, one particular population, neutrophils, was significantly higher from initiation and through progression in R53 compared with PD53 tumors (Figures 2H). In addition, we performed the same line of analysis in two peripheral organs: the spleen and BM. No overall significant differences were observed in the spleen, but in the BM, the fluctuations of these populations between R53- versus PD53-initiated tumors were evident mostly at the 5-week time point but with an opposite trend compared with the profile observed in the brain/tumor (Figure S3). We speculate that populations that are lower in the BM are probably mobilized constantly and recruited to the tumor microenvironment.

Neutrophils infiltrating early-stage tumors limit tumor growth and provide survival benefits

The role and importance of neutrophils in cancer has become clearly noticeable over the past decade, highlighting their anti-tumor and tumor-supporting properties (Shaul and Fridlender, 2019). The higher and steady numbers of neutrophils recruited to R53 tumors (Figure 3A) prompted us to examine their role in glioma progression. We first wanted to find out whether tumor cells ($CD45^{-}/GFP^{+}$) expressed high levels of neutrophil "recruitment signals." Several cytokines and chemokines have been associated previously with neutrophil recruitment, including CXCL1, CXCL2, CCL3, interleukin-1b (IL-1b), granulocyte colonoy-stimulating factor (G-CSF), and intracellular adhesion molecule 1 (ICAM1) (Furze and Rankin, 2008). Indeed, qPCR analysis revealed that all of these genes were upregulated in tumor cells compared with mock-injected normal brain tissue (NBT) controls (Figure 3B). To examine the role of neutrophils *in vivo* at different time points along tumor progression, we first depleted neutrophils at the tumor initiation stage. Mice were injected with the oncogenic lentivirus (this time expressing the luciferase (Luc) reporter; Figure S1A), and 10 days later, neutrophils were depleted by intraperitoneal (i.p.) injection with a neutralizing anti-Ly6G antibody (alternate days over 2 weeks) (Figure 3C). Control mice were injected with the immunoglobulin G2a (IgG2a) isotype control antibody. Ly6G antibody-treated GBM-bearing mice show a dramatic reduction in circulating neutrophils in the first 6 days of treatment compared with GBM-bearing mice that received the IgG2a isotype control (Figures S4A and S4B). These low levels of neutrophils in circulation were also reflected by low scores of neutrophils infiltrating the tumor (Figures S4C and S4D). Depletion of neutrophils at the initiation stage, and only for a short period of time, allowed tumors to develop faster compared with control mice (Figure 3D), resulting in reduced progression-free survival and a median overall survival of 53 days compared with 86 days in control mice (Figure 3E). Histopathology analysis of tumors at the endpoint showed no difference between the treated groups, whereas immunofluorescence staining revealed higher expression of the Ki67 proliferation marker in anti-IgG2a-treated mice (Figures S4E–S4G). Next we performed a similar experiment, but this time depletion of neutrophils was carried out 4 weeks after tumor initiation, when tumors were already well established (Figures S5A–S5C). Bioluminescence imaging showed no significant difference in tumor growth between control and neutrophil-depleted mice (Figure S5D), and no overall survival advantage was evident when neutrophils were depleted after tumors had been established (Figure S5E). Histopathological and immunofluorescence analysis of tumor sections at the endpoint showed no difference between the treated groups (Figures S5F–S5H). These results suggest that "pioneer" neutrophils recruited during tumor initiation have an anti-tumorigenic property; however, this time window is limited, and as the tumor progresses, neutrophils lose their tumor growth control effect.

To further confirm the anti-tumorigenic property of "naive neutrophils" (nNΦs) during the early stages of tumor development, we next performed a modified Winn assay, also known as a tumor neutralization test. For this experiment, we isolated nNΦs or "educated neutrophils" (eNΦs) from the BM of healthy mice or mice bearing R53 tumors, respectively. The

(D) Comparison of $CD4^{+}$ and $CD8^{+}$ T cells subpopulations.
(E and F) Effect of TMZ treatment on immune cell subpopulations in R53 and PD53 tumors. TMZ or vehicle control-treated R53-GSC or PD53-GSC tumors were analyzed for $CD45^{lo}$ and $CD45^{hi}$ total populations (E); the different immune cell populations are indicated in (F).
(G) FACS analyses showing the temporal changes in the $CD45^{hi}CD11b^{+}$ population during tumor progression in R53 versus PD53 tumors.
(H) FACS analysis of macrophages, monocytic myeloid-derived suppressor cells (mMDSCs)/monocytes, neutrophils, and $CD11b^{+}$ dendritic cells (DCs) among $CD45^{+}CD11b^{+}$ populations of GBM tumor-bearing mice. All plots are gated on $CD45^{+}CD11b^{+}$ cells. Mice were euthanized at 2 or 5 weeks after intracranial injections or at the end of the disease for TME analysis.
(A–C) n = 3–5 per group, mean ± SEM, one-way ANOVA with Tukey's HSD (honestly significant difference) post-test.
(E–H) n = 4–5 per group, mean ± SEM, unpaired Student t test.
$p < 0.05$ was considered significant. *$p < 0.05$, **$p < 0.01$, ***$p < 0.001$, ****$p < 0.0001$. ns, not significant. See also Figures S2 and S3.

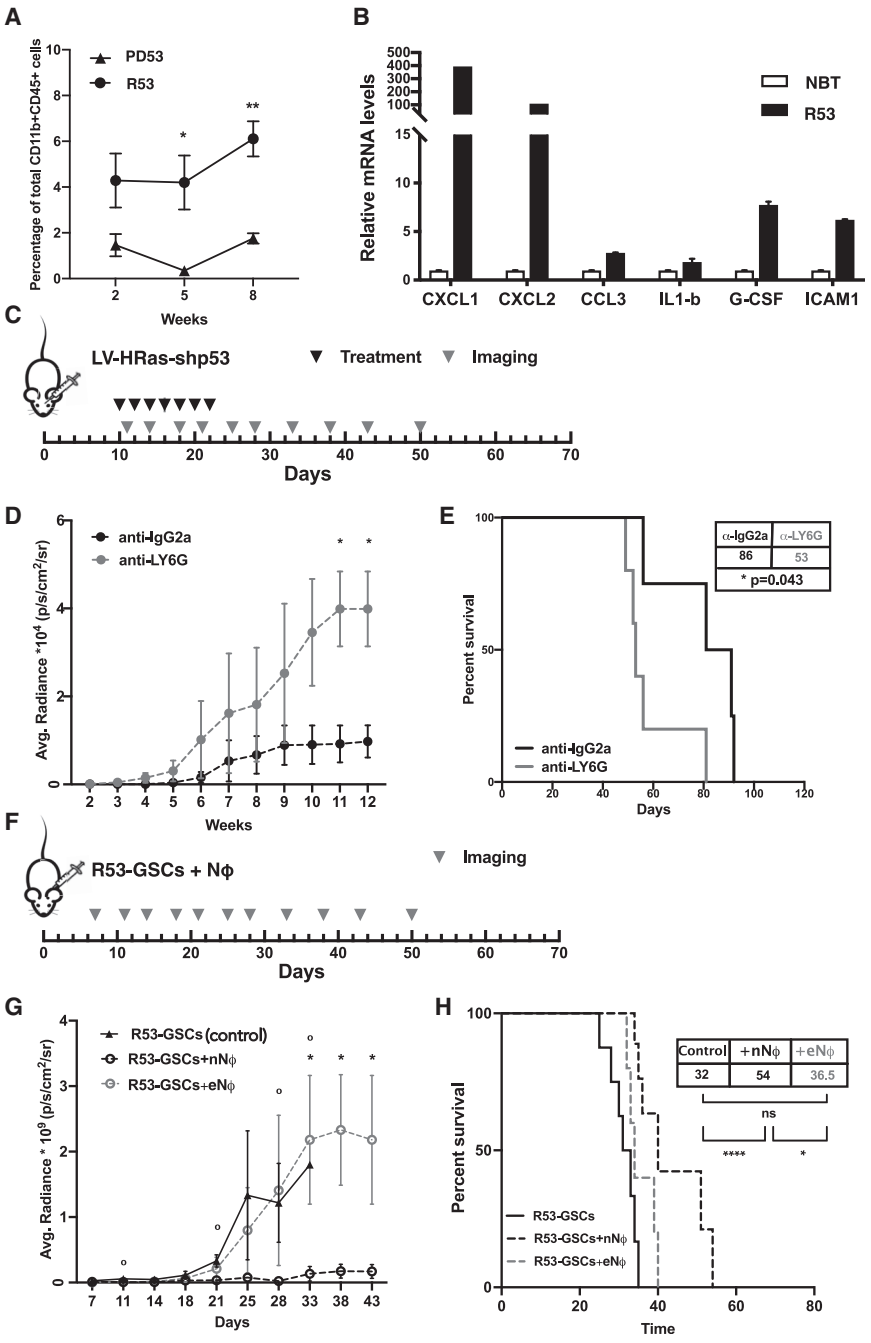

Figure 3. Neutrophils in early tumor stages mediate antitumor resistance

(A) Graph representing the percentage of neutrophils (mean ± SEM) in R53 versus PD53 murine GBM tumors at the indicated time points; n = 3–5 per group, unpaired Student t test.

(B) qRT-PCR analysis of the indicated genes expressed by R53 GBM ($CD45^{-}$/GFP^{+} enriched population) compared with NBT; n = 3.

(C) Schematic of the neutrophil depletion experiment.

(D) Bioluminescence imaging (BLI; Average (Avg.) radiance) of lentivirally (R53) induced R53 tumor growth in neutrophil-depleted (anti-LY6G) and control (anti-IgG2a) mice; n = 5 per group, mean ± SEM, two-way ANOVA.

(E) Kaplan-Meier survival curve of isotype control versus anti-LY6G-treated groups with their median survival and log rank test comparisons.

(F) Experimental scheme of orthotopic co-injection of R53-GSCs-1 Luc^{+} cells with naive neutrophils (nNΦs) or educated neutrophils (eNΦs) (1:1, modified Winn assay). Control, R53-GSCs (1:1 in PBS).

(G) BLI in the modified Winn assay. n = 5 per group, mean ± SEM, two-way ANOVA; °, p value control versus nNΦs; *, p value nNΦs versus eNΦs.

(H) Kaplan-Meier graph representing the overall survival of mice in the modified Winn assay. n = 5 per group; median survival and log-rank test comparisons are indicated in the table.

$p < 0.05$ was considered significant. *$p < 0.05$, **$p < 0.01$, ***$p < 0.001$. Non-significant values are not mentioned. See also Figures S4–S6.

isolated neutrophils were then mixed with R53-GSC and injected into the brain of naive syngeneic mice (Figure 3F). As opposed to the effect of eNΦs on tumor progression and survival, nNΦs significantly inhibited tumor growth and elongated overall survival (Figures 3G and 3H). Tumor sections analyzed at the endpoint showed lower Ki67 staining when tumor cells were co-injected with nNΦs (Figure S6). These *in vivo* observations uncover a powerful anti-tumorigenic effect of neutrophils, which is most significant early during tumor establishment.

nNΦs are cytotoxic, whereas eNΦs are immunosuppressive

The short half-life of blood neutrophils and their low numbers in the blood (~3–5 × 10^5 cells/mL) and tumors (5% of total $CD11b^{+}CD45^{high}$) notwithstanding, their phenotypic switch leading to opposing tumor outcomes prompted us to explore the function of neutrophils obtained from BM of healthy versus tumor-bearing mice. Neutrophil production occurs primarily in the BM, where most stages of maturation take place (Pillay et al., 2013). Morphological characteristics, such as nuclear segmentation, are considered the most accurate for immature/mature neutrophil identification, with band nuclei representing immature neutrophils and segmented nuclei the mature state (Mackey et al., 2019). Therefore, we first analyzed the morphology of neutrophils isolated from the BM of healthy (nNΦs) and R53-tumor bearing mice (eNΦs). We found that the eNΦ population isolated from the BM of mice with R53 tumors has a higher ratio of immature NΦs compared with nNΦs (Figures 4A and 4B). These findings are in line with previous studies reporting the existence of immature neutrophils in mouse models of solid cancers and

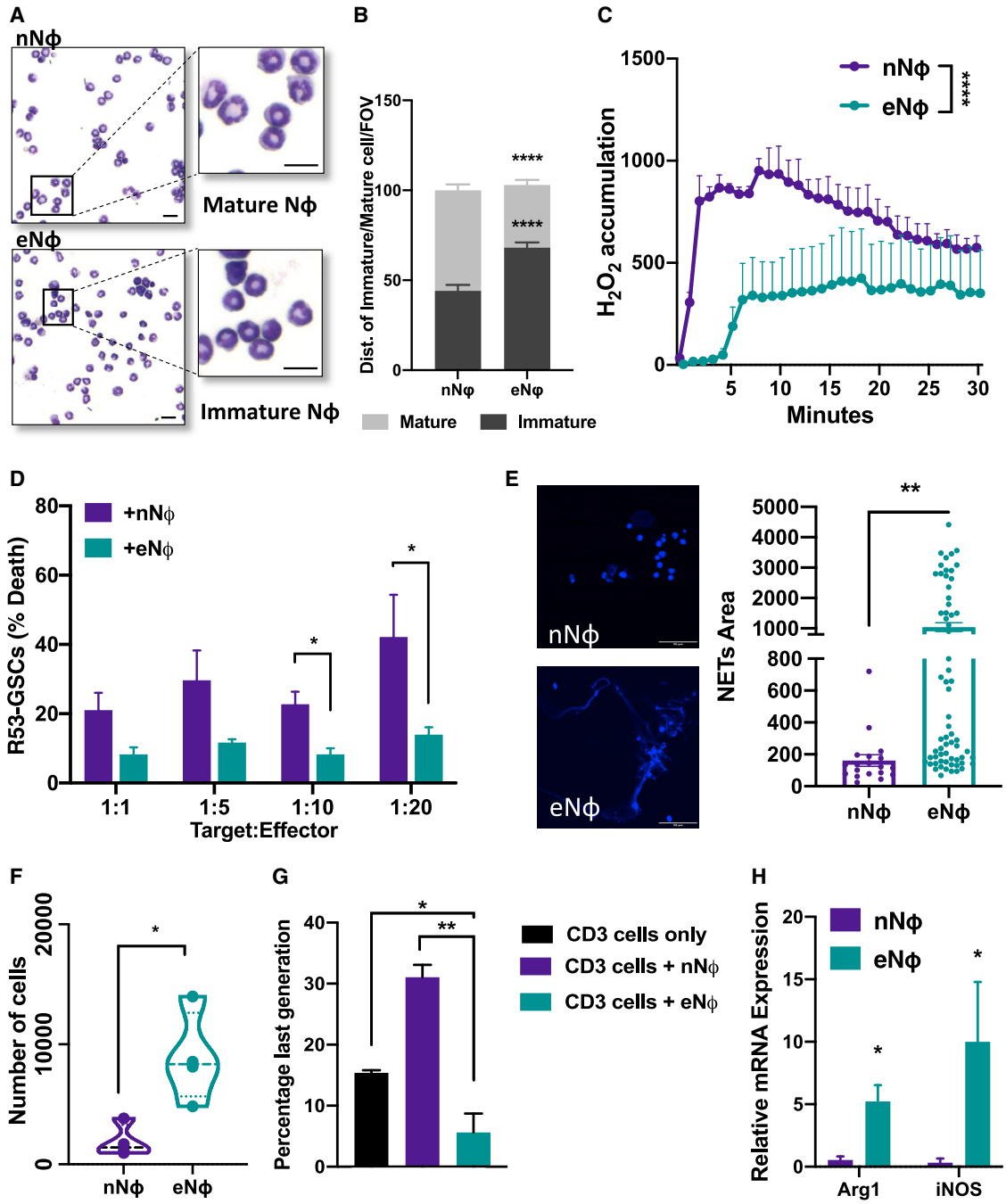

Figure 4. BM eNΦs display a pro-tumorigenic phenotype *in vitro*

(A) Representative cytospin images of BM-derived nNΦs and eNΦs. Scale bar, 10 μm.

(B) Quantification of immature/mature neutrophil ratio. n = 3; the graph represents mean ± SEM, unpaired Student's t test.

(C) H_2O_2 production by PMA-stimulated nNΦs and eNΦs.

(D) Cytotoxicity effect of nNΦs and eNΦs when co-cultured with R53-GSC at the indicated target:effector ratios.

(E) Representative DAPI-stained (blue) confocal microscopy images of conditioned medium (CM)-induced NETosis in nNΦs and eNΦs. Scale bar, 50 μm. The graph on the right shows quantification of NET formation (normalized to medium control)/FOV (field of view).

(F) Quantification of migrating neutrophils toward glioma CM.

(G) *In vitro* T cell proliferation, measured by reduction of cell tracer dilution assay when co-cultured with nNΦs or eNΦs (1:1). The graph represents quantification of the percentage of cells in the last generation.

(H) qPCR analysis of Arg1 and iNOS mRNA expression levels in nNΦs and eNΦs; n = 3 per group. Mean ± SEM, unpaired Student t test.

All experiments were repeated 3 times and performed on neutrophils from the BM of tumor (R53-GSCs)-bearing mice and healthy control mice separately. $p < 0.05$ was considered significant. *$p < 0.05$, **$p < 0.01$, ****$p < 0.0001$. See also Figure S7.

individuals with lung, breast, and ovarian cancer (Mackey et al., 2019). Although most studies focus on the properties of TANs/PMN MDSC, little is known about the characteristics of BM-derived neutrophils in brain tumors. We therefore examined the *ex vivo* functional differences between BM-derived nNΦs and eNΦs in two independent R53 glioma models, starting with reactive oxygen species (ROS) production, an important player in neutrophil effector mechanisms (Powell and Huttenlocher, 2016). Evaluation of basal production of ROS showed a tendency for higher levels in eNΦs compared with nNΦs (Figure S7A). However, upon stimulation with phorbol 12-myristate 13-acetate (PMA), which induces nicotinamide adenine dinucleotide phosphate (NADPH)-oxidase activity, nNΦs showed higher levels of ROS production compared with eNΦs (Figure 4C; Figure S7B). ROS production is a powerful antimicrobial weapon, but in the context of cancer, ROS release is correlated with the capacity to directly kill tumor cells (Uribe-Querol and Rosales, 2015). Indeed, the increased levels of ROS released under maximum stimulus conditions (PMA) resulted in significantly higher cytotoxic effects when nNΦs were co-cultured with MES glioma cells (Figure 4D; Figure S7C), supporting the anti-tumorigenic properties of nNΦs. Neutrophil extracellular traps (NETs) can be released by neutrophils following their activation (Kaplan and Radic, 2012), favoring tumor growth (Demers et al., 2016). Although conditioned medium (CM) of R53 glioma cells induced NET formation when added to nNΦs, this effect was more pronounced when the same CM was added to eNΦs (Figure 4E; Figure S7D). Another difference we observed between nNΦs and eNΦs is their capacity to migrate toward CM from R53 glioma cells. The increased capacity of eNΦs to migrate toward CM obtained from R53 glioma cells can explain the higher numbers of recruited neutrophils along R53-induced tumor progression as well as the fast mobilization of neutrophils from the BM in R53 tumors (Figure 4F; Figure S7E). We also noticed that, although BM nNΦs have an average half-life of less than 24 h when cultured *in vitro*, BM eNΦs maintained over 10-fold more viable cells for an extended period of time (18 h versus 36 h, respectively (Figure S7F). Finally, we evaluated the effect of nNΦs and eNΦs on T cell proliferation. PMN MDSC/TANs have been widely reported to suppress T cell proliferation (Granot, 2019; Michaeli et al., 2017). Our results show that BM-derived eNΦs have an immunosuppressive effect on activated T cells (Figure 4G; Figure S7G), and this effect correlates with higher levels of expression of *Arginase 1* (*Arg1)* and *inducible nitric oxide synthase* (*iNOS)* in eNΦs, both associated previously with T cell suppression (Rodriguez et al., 2004; Figure 4H).

Our observations demonstrate that BM-derived neutrophils respond to tumor-derived factors, causing their phenotypic switch from the anti-tumorigenic, highly cytotoxic phenotype supporting T cell proliferation to a less cytotoxic, T cell-suppressive phenotype supporting tumor progression.

BM-derived eNΦs induce tumor angiogenesis

PMN MDSC/TANs display several pro-tumor functions, including their ability to support angiogenesis. To examine the role of BM-derived eNΦs in angiogenesis, we went back to our modified Winn assay and compared the density of blood vessels in the different tumors. Confocal microscopy analysis of tumor sections stained with the endothelial marker von Willebrand factor (vWF) revealed not only higher blood vessel density but also different morphology and higher disorganization of tumor vasculature in R53 tumors co-injected with BM-derived eNΦs compared with those co-injected with BM nNΦs (Figure 5A). The same analysis was performed in the neutrophil depletion experiment, revealing that early depletion of anti-tumorigenic neutrophils resulted in higher blood vessel density in the tumor, but no difference was observed at the later time point (Figures S8A and S8B). GBM is one of the most vasculature-rich tumors, and in addition to the regular mechanisms of tumor vasculature formation, we previously identified generation of tumor-derived endothelial cells (TDECs) from GSCs (Soda et al., 2011). Under hypoxic conditions and as the tumor progresses, TDECs become a significant fraction of the total endothelial cell population in the deep area of the lesions (Soda et al., 2011). Here we show that, although 005 TDECs form tubular networks when co-cultured with eNΦs on Matrigel, decreased tubular network formation was observed in the presence of nNΦs (Figure 5B). To better characterize the pro-angiogenic feature of eNΦs, we carried out whole-transcriptome analysis on mRNA isolated from BM-derived nNΦs and eNΦs. RNA-seq analysis showed 1,755 genes differentially expressed between nNΦs and eNΦs (Figure 5C) and Gene Ontology (GO) analysis revealed biological pathways associated with angiogenesis (Figure 5D, underlined). To validate the sequencing results, we performed qPCR analysis of classically known neutrophil-associated angiogenic markers such as *transforming growth factor-beta (TGFβ)*, *matrix metallopeptidase 9 (MMP9)*, and vascular endothelial growth factor alpha (*VEGFα)* (Granot, 2019; Figure S8C). These results further support the angiogenic potency of BM-derived eNΦs.

Neutrophilia correlates with poor overall survival in individuals with malignant glioma

To further support the human relevance of our findings, we analyzed human datasets of individuals with glioma. Indeed, compared with NBT, GBM has significantly higher infiltration of neutrophils (Figure 6A; analyzed using cell-type identification by estimating relative subsets of RNA transcripts [CIBERSORT]; Newman et al., 2015). Moreover, scRNA-seq analysis comparing immune cell fractions among different molecular GBM subtypes has revealed significantly higher levels of neutrophil infiltration in MES versus PN tumors (Wang et al., 2017). Transcriptomics analyses of MES and PN tumors (TCGA) further support these results by showing significantly higher expression of cytokines and chemokines known to recruit neutrophils in MES tumors (Figure 6B), similar to the observations obtained in our study (compare with Figure 3B). Pathway analysis using gene set enrichment analysis (GSEA) also revealed enrichment of a neutrophil-related gene set (Figure 6C). GO analysis of the highly ranked (adjusted p value [p-adjust] < 0.05) differentially expressed genes in the GSEA revealed biological processes, including "inflammatory response," "vascular endothelial growth factor receptor signaling," and "cytokine secretion," to be overrepresented significantly (corrected $p < 0.05$) in MES tumors. These enriched biological processes in human-associated neutrophils support the results we obtained in our *ex vivo* experiments with murine eNΦs compared with nNΦs (Figure 6D, underlined in red). Finally, neutrophilia

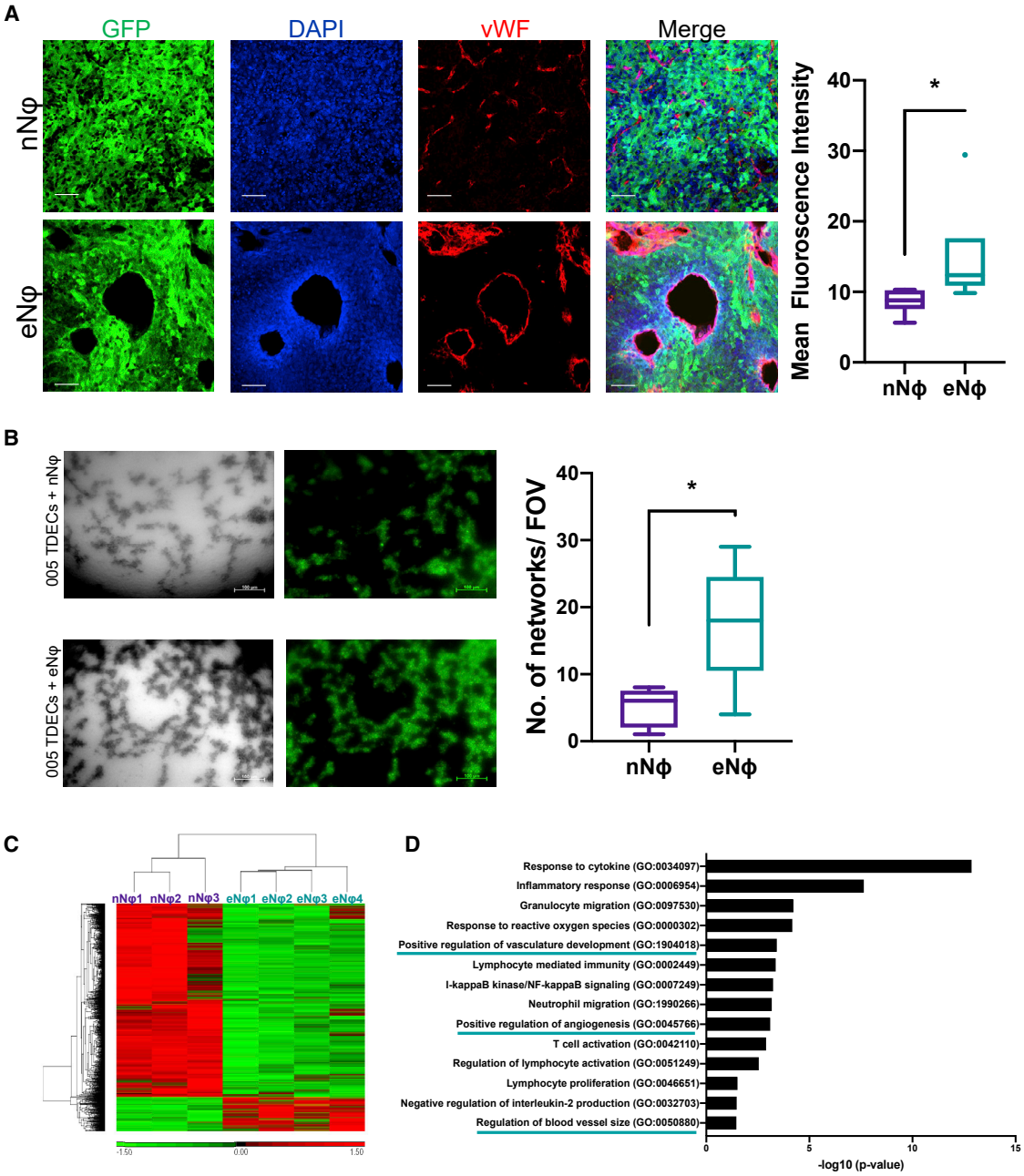

Figure 5. BM "educated" neutrophils promote angiogenesis

(A) Immunofluorescence images representing the vasculature (vWF) in R53 glioma tumors co-injected with nNΦs or eNΦs. Scale bar, 100 μm. Quantification of blood vessels/FOV; n = 3.

(B) *In vitro* tube formation assay of 005 TDECs co-cultured with nNΦs or eNΦs. Scale bar = 100 μm. Quantification of closed network/FOV, n = 3 n. Mean ± SEM, unpaired Student t test.

(C) Heatmap showing differential transcriptional profile of BM-derived nNΦs (n = 3) and R53 eNΦs (n = 4). Differentially expressed genes (ANOVA, $p < 0.05$; fold change cutoff 1.5) are shown.

(D) GO enrichment analysis using differentially expressed genes between nNΦs versus eNΦs in (C)

$p < 0.05$ was considered significant. *$p < 0.05$. See also Figure S8.

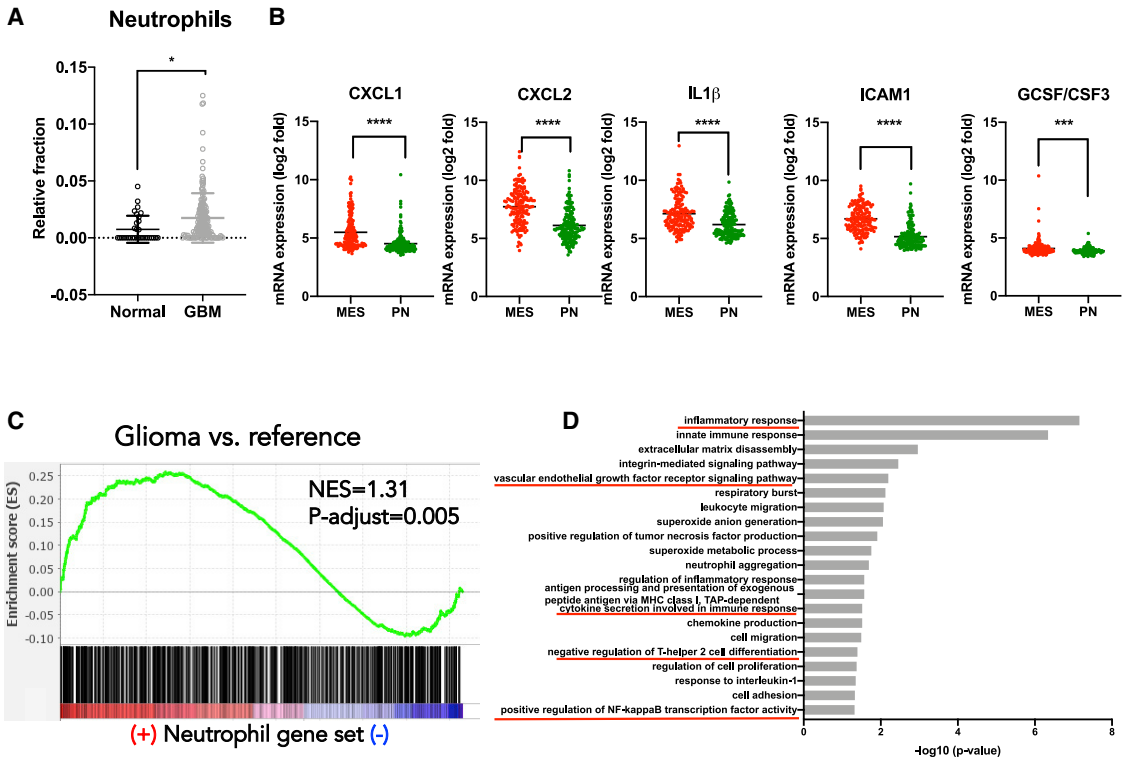

Figure 6. Validation of neutrophil infiltration in human GBM

(A) CIBERSORT analysis showing enrichment of neutrophils in human GBM compared with NBT (TCGA dataset).

(B) mRNA expression of the indicated genes in the TCGA database comparing MES versus PN glioma. Mean ± SEM, unpaired Student's t test. $p < 0.05$ was considered significant. *$p < 0.05$, ***$p < 0.001$, ****$p < 0.0001$.

(C) Ranked gene set enrichment analysis (GSEA) was performed to compare only differentially expressed genes (DEGs) matched with the human neutrophil signature (The Molecular Signature Database).

(D) Significantly enriched Gene Ontology (GO) terms of DEGs associated with neutrophils in human GBM. NES, normalized enrichment score.

being associated with the worst overall survival in malignant gliomas supports an important role of neutrophils and their plasticity in gliomagenesis (Bambury et al., 2013; Wiencke et al., 2017).

DISCUSSION

Immunotherapy has permanently changed the cancer treatment landscape, and with this modality showing successful clinical outcomes, it has renewed interest in the role of the immune milieu in tumor initiation and progression. Longitudinal analysis of TME changes is very difficult in human GBM because of the lack of available material. Transcriptomics analysis at the single-cell level and comparing primary tumors with recurrent tumors revealed variations in the frequency of certain immune populations infiltrating different molecular GBM subtypes (Wang et al., 2017). Using different approaches, studies of human samples have demonstrated that higher numbers of TAMs infiltrate MES GBM (Beier et al., 2012; Engler et al., 2012; Kaffes et al., 2019; Martinez-Lage et al., 2019; Sørensen et al., 2018). Additional evidence of differences in TAM infiltration and mutational load in glioma has been reported in a study comparing human isocitrate dehydrogenase 1 mutant (*IDH* mut) and IDH wild type (*IDH* WT) gliomas. Mutations in this metabolic enzyme are generally found in low-grade gliomas (grades II–III) and have a better prognosis than high-grade IV *IDH* WT GBM (Klemm et al., 2020). All of these studies have been very instrumental in defining the immunological architecture of brain tumors in relation to the genomic tumor profile. However, they do not allow further examination of the causative roles played by each of the infiltrating immune cell populations in tumor initiation and progression.

Using a Cre-inducible lentiviral GBM mouse model, we were previously able to recapitulate the histopathological characteristics and molecular signature of the human disease (Friedmann-Morvinski et al., 2012; Marumoto et al., 2009). In this study, we used this GBM model to interrogate the longitudinal immune landscape of tumors initiated from different oncogenic drivers. Our findings support the notion that inter-tumor heterogeneity and complexity go beyond the tumor cells and are reflected by the immune cells in the tumor microenvironment (Friebel et al., 2020; Kaffes et al., 2019; Klemm et al., 2020; Martinez-Lage et al., 2019; Wang et al., 2017). Our analyses at the endpoint revealed that TAMs account for the majority of $CD45^{+high}$ immune cells in the R53-GBM tumor mass and are in line with previous studies using murine models and human samples (Chen et al., 2017; Kaffes et al., 2019). TAMs are the most reported and

well-characterized immune cells to have pro-tumorigenic functions in the TME and have been shown to increase in tumors over time in mice and humans (Binnewies et al., 2018). Attempts to interfere with recruitment of TAMs in preclinical models of GBM prolonged the survival of tumor-bearing mice (Chen et al., 2017). Besides TAMs, other myeloid and lymphoid cells have been reported to infiltrate the GBM parenchyma (Quail and Joyce, 2017). Here we identify neutrophils to preferentially infiltrate R53-induced tumors modeling human MES GBM and reveal that early tumor-infiltrating neutrophils possess anti-tumor capacities, but these are lost as tumors progress.

In the past decade, the role of neutrophils has extended from its essential effector function in inflammatory response and defense against pathogenic organisms to a much broader role in coordinating innate and adaptive immune responses (Mantovani et al., 2011). In cancer, neutrophils are mostly associated with a pro-tumoral function, and neutrophilia and an elevated ratio of blood neutrophils to lymphocytes (NLR) are associated with a poor prognosis (Shen et al., 2014; Templeton et al., 2014). In gliomas, there is experimental and clinical evidence indicating that neutrophils promote glioma cell proliferation, support GSCs exhibiting self-renewing capacity, and facilitate angiogenesis and resistance to therapy (Khan et al., 2020). Most of the evidence stems from circulating neutrophils and PMN MDSC/TANs at late stages of tumor development, with the mechanisms involved in these effects still under investigation.

In the present study, we report that neutrophils infiltrate R53 tumors from initiation through progression, peaking at the endpoint. We confirmed that R53 tumors express the relevant cues to actively recruit neutrophils, such as *CXCL1*, *CXCL2*, and *G-CSF*, with the latter favoring BM hematopoiesis toward the granulocyte lineage and away from lymphocyte differentiation (Massara et al., 2017). To address the functional role of early-recruited neutrophils versus late-infiltrating neutrophils, we depleted neutrophils at two different time points in tumor development. Tumors grew faster when neutrophils were depleted at the initiation stage, suggesting that early tumor-infiltrating neutrophils possess anti-tumorigenic properties and are indeed recruited to prevent tumor progression. However, depletion at a later stage, corresponding to a well-established tumor, had no significant effect on GBM progression in our MES GBM model. Depletion of gMDSCs with the anti-Ly6G antibody has been shown recently to provide survival benefits in a GL261 syngeneic model of GBM; however, the time window of neutralizing antibody injection, tumor size, tumor model, and sex of the mice can explain the different outcome (Bayik et al., 2020). Neutrophil heterogeneity and plasticity are well documented, and neutrophil-like populations have been recognized to play different roles in cancer development (Jaillon et al., 2020). Neutrophils from the blood of individuals with cancer have been classified in different subsets based on their density, with normal-density neutrophils (NDNs) associated with cytotoxic anti-tumor effects and mature and immature low-density neutrophils (LDNs) with immunosuppressive pro-tumor properties (Granot, 2019; Sagiv et al., 2015). Neutrophils found at tumor sites can be polarized toward tumor-inhibiting (N1) or -promoting (N2) phenotypes, similar to the dynamic states of anti- and pro-tumoral macrophages (M1 and M2). Less in known about the phenotype and functional role of BM-derived neutrophils, especially in brain tumors. Our results revealed that BM neutrophils derived from glioma-bearing mice (eNΦs) are predominantly in an immature state compared with BM neutrophils isolated from healthy mice (nNΦs). The functional properties and relevance of immature neutrophils remains understudied in cancer. Here we showed that BM-derived eNΦs are pre-committed and possess a pro-tumor functional property, supported by their pro-angiogenic and T cell immunosuppressive effects. Although *in vivo* (Winn assay) and *in vitro* assays using BM-derived nNΦs showed cytotoxic and anti-tumorigenic properties, BM eNΦs showed an opposite effect, suggesting a phenotypic switch even before these cells reach the tumor and become exposed to the tumor microenvironment. These results suggest systemic regulation of immune cells by GBM prior to their recruitment and mobilization to the tumor area. Immune-cancer cell interactions at the tumor site have been mostly investigated, whereas the systemic immune changes at distant microenvironments and their effects on tumor growth remains poorly explored. Evidence of cross-talk between lung tumors and bones has been reported previously in a very elegant study showing activation of osteoblastic cells and subsequent induction of pro-tumorigenic neutrophils (Engblom et al., 2017). In breast cancer, tumor production of G-CSF induces activation of myeloid differentiation in the BM, which, in turn, leads to generation of immunosuppressive neutrophils (Casbon et al., 2015). Systemic immune perturbations have been shown recently across several cancer models, with neutrophils among the immune populations showing continuous increase during cancer development (Allen et al., 2020). Our results are in line with these observations and suggest systemic immune remodeling of neutrophils in GBM despite its localization in the brain. How brain tumor cells orchestrate mobilization, recruitment, and polarization of neutrophils is currently under investigation. Lessons from other types of tumors indicate that molecules that control release of neutrophils from the BM are upregulated in tumor cells and tumor-associated cells in the TME or systemically (Coffelt et al., 2016). Our results indicate that signals emanating from cancer cells, such as CXCL1, CXCL2, and G-CSF, play an important role in mobilization and release of neutrophils from the BM, even of NΦs in an immature state. We can only speculate at this point that, in addition to these factors, tumor cells regulate the expression of (or override) other molecules responsible for retention of neutrophils in the BM (e.g., CXCL12). Our *ex vivo* data suggest different functional properties between BM-derived immature eNΦs and mature nNΦs, suggesting that neutrophil polarization begins early during granulopoiesis in the BM. Whether these distinct populations are committed to their final fate or further polarization occurs when reaching the tumor site remains undetermined. Unveiling the mechanisms of systemic immune dysfunction, including neutrophil reprogramming, will not only help predict progression of the tumors but can also help to better predict the outcome of immunotherapy.

STAR★METHODS

Detailed methods are provided in the online version of this paper and include the following:

- KEY RESOURCES TABLE

SUPPLEMENTAL INFORMATION

Supplemental information can be found online at https://doi.org/10.1016/j.celrep.2021.109480.

ACKNOWLEDGMENTS

We thank Dr. Victoria Marcus for help with H&E staining of neutrophils, Prof. Tal Burstyn-Cohen for critically reading the manuscript, and Shreoshi Sengupta and Dr. Metsada Pasmanik-Chor for bioinformatics assistance. This research was supported by grants to D.F-M. from the Israel Science Foundation (1310/15), the Broad-ISF (24/17), the Israel Cancer Research Fund (Research Career Development Award), and the Fritz Thyssen Foundation.

AUTHOR CONTRIBUTIONS

D.F.-M. and P.M. designed the research. P.M., L.A., I.M., L.R.-N., and D.F.-M. performed the experiments. P.M. and D.F.-M. analyzed the results. G.S. and N.S. analyzed the tumor RNA-seq data. P.M. and D.F.-M. wrote the manuscript.

DECLARATION OF INTERESTS

The authors declare no competing interests.

Received: September 29, 2020
Revised: March 17, 2021
Accepted: July 13, 2021
Published: August 3, 2021

REFERENCES

Allen, B.M., Hiam, K.J., Burnett, C.E., Venida, A., DeBarge, R., Tenvooren, I., Marquez, D.M., Cho, N.W., Carmi, Y., and Spitzer, M.H. (2020). Systemic dysfunction and plasticity of the immune macroenvironment in cancer models. Nat. Med. *26*, 1125–1134.

Amankulor, N.M., Kim, Y., Arora, S., Kargl, J., Szulzewsky, F., Hanke, M., Margineantu, D.H., Rao, A., Bolouri, H., Delrow, J., et al. (2017). Mutant IDH1 regulates the tumor-associated immune system in gliomas. Genes Dev. *31*, 774–786.

Angel, I., Pilo Kerman, O., Rousso-Noori, L., and Friedmann-Morvinski, D. (2020). Tenascin C promotes cancer cell plasticity in mesenchymal glioblastoma. Oncogene *39*, 6990–7004.

Ashburner, M., Ball, C.A., Blake, J.A., Botstein, D., Butler, H., Cherry, J.M., Davis, A.P., Dolinski, K., Dwight, S.S., Eppig, J.T., et al.; The Gene Ontology Consortium (2000). Gene ontology: tool for the unification of biology. Nat. Genet. *25*, 25–29.

Bambury, R.M., Teo, M.Y., Power, D.G., Yusuf, A., Murray, S., Battley, J.E., Drake, C., O'Dea, P., Bermingham, N., Keohane, C., et al. (2013). The association of pre-treatment neutrophil to lymphocyte ratio with overall survival in patients with glioblastoma multiforme. J. Neurooncol. *114*, 149–154.

Bayik, D., Zhou, Y., Park, C., Hong, C., Vail, D., Silver, D.J., Lauko, A., Roversi, G., Watson, D.C., Lo, A., et al. (2020). Myeloid-Derived Suppressor Cell Subsets Drive Glioblastoma Growth in a Sex-Specific Manner. Cancer Discov. *10*, 1210–1225.

Beier, C.P., Kumar, P., Meyer, K., Leukel, P., Bruttel, V., Aschenbrenner, I., Riemenschneider, M.J., Fragoulis, A., Rümmele, P., Lamszus, K., et al. (2012). The cancer stem cell subtype determines immune infiltration of glioblastoma. Stem Cells Dev. *21*, 2753–2761.

Binnewies, M., Roberts, E.W., Kersten, K., Chan, V., Fearon, D.F., Merad, M., Coussens, L.M., Gabrilovich, D.I., Ostrand-Rosenberg, S., Hedrick, C.C., et al. (2018). Understanding the tumor immune microenvironment (TIME) for effective therapy. Nat. Med. *24*, 541–550.

Borregaard, N. (2010). Neutrophils, from marrow to microbes. Immunity *33*, 657–670.

Brandenburg, S., Turkowski, K., Mueller, A., Radev, Y.T., Seidlitz, S., and Vajkoczy, P. (2017). Myeloid cells expressing high level of CD45 are associated with a distinct activated phenotype in glioma. Immunol. Res. *65*, 757–768.

Casbon, A.J., Reynaud, D., Park, C., Khuc, E., Gan, D.D., Schepers, K., Passegué, E., and Werb, Z. (2015). Invasive breast cancer reprograms early myeloid differentiation in the bone marrow to generate immunosuppressive neutrophils. Proc. Natl. Acad. Sci. USA *112*, E566–E575.

Charles, N.A., Holland, E.C., Gilbertson, R., Glass, R., and Kettenmann, H. (2011). The brain tumor microenvironment. Glia *59*, 1169–1180.

Chen, Z., Feng, X., Herting, C.J., Garcia, V.A., Nie, K., Pong, W.W., Rasmussen, R., Dwivedi, B., Seby, S., Wolf, S.A., et al. (2017). Cellular and Molecular Identity of Tumor-Associated Macrophages in Glioblastoma. Cancer Res. *77*, 2266–2278.

Chen, S., Zhou, Y., Chen, Y., and Gu, J. (2018). fastp: an ultra-fast all-in-one FASTQ preprocessor. Bioinformatics *34*, i884–i890.

Coffelt, S.B., Wellenstein, M.D., and de Visser, K.E. (2016). Neutrophils in cancer: neutral no more. Nat. Rev. Cancer *16*, 431–446.

Demers, M., Wong, S.L., Martinod, K., Gallant, M., Cabral, J.E., Wang, Y., and Wagner, D.D. (2016). Priming of neutrophils toward NETosis promotes tumor growth. OncoImmunology *5*, e1134073.

Dobin, A., Davis, C.A., Schlesinger, F., Drenkow, J., Zaleski, C., Jha, S., Batut, P., Chaisson, M., and Gingeras, T.R. (2013). STAR: ultrafast universal RNA-seq aligner. Bioinformatics *29*, 15–21.

Engblom, C., Pfirschke, C., Zilionis, R., Da Silva Martins, J., Bos, S.A., Courties, G., Rickelt, S., Severe, N., Baryawno, N., Faget, J., et al. (2017). Osteoblasts remotely supply lung tumors with cancer-promoting SiglecF^{high} neutrophils. Science *358*, eaal5081.

Engler, J.R., Robinson, A.E., Smirnov, I., Hodgson, J.G., Berger, M.S., Gupta, N., James, C.D., Molinaro, A., and Phillips, J.J. (2012). Increased microglia/macrophage gene expression in a subset of adult and pediatric astrocytomas. PLoS ONE *7*, e43339.

Fedele, M., Cerchia, L., Pegoraro, S., Sgarra, R., and Manfioletti, G. (2019). Proneural-Mesenchymal Transition: Phenotypic Plasticity to Acquire Multitherapy Resistance in Glioblastoma. Int. J. Mol. Sci. *20*, 2746.

Friebel, E., Kapolou, K., Unger, S., Nunez, N.G., Utz, S., Rushing, E.J., Regli, L., Weller, M., Greter, M., Tugues, S., et al. (2020). Single-Cell Mapping of Human Brain Cancer Reveals Tumor-Specific Instruction of Tissue-Invading Leukocytes. Cell *181*, 1626–1642.e20.

Friedmann-Morvinski, D., and Singer, O. (2013). Overexpression Models: Lentiviral Modeling of Brain Cancer. Curr. Protoc. Mouse Biol. *3*, 121–139.

Friedmann-Morvinski, D., and Verma, I.M. (2014). Dedifferentiation and reprogramming: origins of cancer stem cells. EMBO Rep. *15*, 244–253.

Friedmann-Morvinski, D., Bushong, E.A., Ke, E., Soda, Y., Marumoto, T., Singer, O., Ellisman, M.H., and Verma, I.M. (2012). Dedifferentiation of neurons and astrocytes by oncogenes can induce gliomas in mice. Science *338*, 1080–1084.

Friedmann-Morvinski, D., Narasimamurthy, R., Xia, Y., Myskiw, C., Soda, Y., and Verma, I.M. (2016). Targeting NF-κB in glioblastoma: A therapeutic approach. Sci. Adv. *2*, e1501292.

Furnari, F.B., Fenton, T., Bachoo, R.M., Mukasa, A., Stommel, J.M., Stegh, A., Hahn, W.C., Ligon, K.L., Louis, D.N., Brennan, C., et al. (2007). Malignant astrocytic glioma: genetics, biology, and paths to treatment. Genes Dev. *21*, 2683–2710.

Furze, R.C., and Rankin, S.M. (2008). Neutrophil mobilization and clearance in the bone marrow. Immunology *125*, 281–288.

Gabrusiewicz, K., Rodriguez, B., Wei, J., Hashimoto, Y., Healy, L.M., Maiti, S.N., Thomas, G., Zhou, S., Wang, Q., Elakkad, A., et al. (2016). Glioblastoma-infiltrated innate immune cells resemble M0 macrophage phenotype. JCI Insight *1*, e85841.

Glass, R., and Synowitz, M. (2014). CNS macrophages and peripheral myeloid cells in brain tumours. Acta Neuropathol. *128*, 347–362.

Granot, Z. (2019). Neutrophils as a Therapeutic Target in Cancer. Front. Immunol. *10*, 1710.

Gu, Z., Eils, R., and Schlesner, M. (2016). Complex heatmaps reveal patterns and correlations in multidimensional genomic data. Bioinformatics *32*, 2847–2849.

Hambardzumyan, D., Gutmann, D.H., and Kettenmann, H. (2016). The role of microglia and macrophages in glioma maintenance and progression. Nat. Neurosci. *19*, 20–27.

Huang, W., Sherman, B.T., and Lempicki, R.A. (2009). Systematic and integrative analysis of large gene lists using DAVID bioinformatics resources. Nat. Protoc. *4*, 44–57.

Jaillon, S., Ponzetta, A., Di Mitri, D., Santoni, A., Bonecchi, R., and Mantovani, A. (2020). Neutrophil diversity and plasticity in tumour progression and therapy. Nat. Rev. Cancer *20*, 485–503.

Kaffes, I., Szulzewsky, F., Chen, Z., Herting, C.J., Gabanic, B., Velázquez Vega, J.E., Shelton, J., Switchenko, J.M., Ross, J.L., McSwain, L.F., et al. (2019). Human Mesenchymal glioblastomas are characterized by an increased immune cell presence compared to Proneural and Classical tumors. OncoImmunology *8*, e1655360.

Kaplan, M.J., and Radic, M. (2012). Neutrophil extracellular traps: double-edged swords of innate immunity. J. Immunol. *189*, 2689–2695.

Khan, S., Mittal, S., McGee, K., Alfaro-Munoz, K.D., Majd, N., Balasubramaniyan, V., and de Groot, J.F. (2020). Role of Neutrophils and Myeloid-Derived Suppressor Cells in Glioma Progression and Treatment Resistance. Int. J. Mol. Sci. *21*, 1954.

Klemm, F., Maas, R.R., Bowman, R.L., Kornete, M., Soukup, K., Nassiri, S., Brouland, J.P., Iacobuzio-Donahue, C.A., Brennan, C., Tabar, V., et al. (2020). Interrogation of the Microenvironmental Landscape in Brain Tumors Reveals Disease-Specific Alterations of Immune Cells. Cell *181*, 1643–1660.e17.

Lathia, J.D., Mack, S.C., Mulkearns-Hubert, E.E., Valentim, C.L., and Rich, J.N. (2015). Cancer stem cells in glioblastoma. Genes Dev. *29*, 1203–1217.

Love, M.I., Huber, W., and Anders, S. (2014). Moderated estimation of fold change and dispersion for RNA-seq data with DESeq2. Genome Biol. *15*, 550.

Mackey, J.B.G., Coffelt, S.B., and Carlin, L.M. (2019). Neutrophil Maturity in Cancer. Front. Immunol. *10*, 1912.

Mantovani, A., Cassatella, M.A., Costantini, C., and Jaillon, S. (2011). Neutrophils in the activation and regulation of innate and adaptive immunity. Nat. Rev. Immunol. *11*, 519–531.

Martinez-Lage, M., Lynch, T.M., Bi, Y., Cocito, C., Way, G.P., Pal, S., Haller, J., Yan, R.E., Ziober, A., Nguyen, A., et al. (2019). Immune landscapes associated with different glioblastoma molecular subtypes. Acta Neuropathol. Commun. *7*, 203.

Marumoto, T., Tashiro, A., Friedmann-Morvinski, D., Scadeng, M., Soda, Y., Gage, F.H., and Verma, I.M. (2009). Development of a novel mouse glioma model using lentiviral vectors. Nat. Med. *15*, 110–116.

Marziali, G., Signore, M., Buccarelli, M., Grande, S., Palma, A., Biffoni, M., Rosi, A., D'Alessandris, Q.G., Martini, M., Larocca, L.M., et al. (2016). Metabolic/Proteomic Signature Defines Two Glioblastoma Subtypes With Different Clinical Outcome. Sci. Rep. *6*, 21557.

Massara, M., Persico, P., Bonavita, O., Mollica Poeta, V., Locati, M., Simonelli, M., and Bonecchi, R. (2017). Neutrophils in Gliomas. Front. Immunol. *8*, 1349.

McCarthy, D.J., Chen, Y., and Smyth, G.K. (2012). Differential expression analysis of multifactor RNA-Seq experiments with respect to biological variation. Nucleic Acids Res. *40*, 4288–4297.

Michaeli, J., Shaul, M.E., Mishalian, I., Hovav, A.H., Levy, L., Zolotriov, L., Granot, Z., and Fridlender, Z.G. (2017). Tumor-associated neutrophils induce apoptosis of non-activated CD8 T-cells in a TNFα and NO-dependent mechanism, promoting a tumor-supportive environment. OncoImmunology *6*, e1356965.

Müller, A., Brandenburg, S., Turkowski, K., Müller, S., and Vajkoczy, P. (2015). Resident microglia, and not peripheral macrophages, are the main source of brain tumor mononuclear cells. Int. J. Cancer *137*, 278–288.

Neftel, C., Laffy, J., Filbin, M.G., Hara, T., Shore, M.E., Rahme, G.J., Richman, A.R., Silverbush, D., Shaw, M.L., Hebert, C.M., et al. (2019). An Integrative Model of Cellular States, Plasticity, and Genetics for Glioblastoma. Cell *178*, 835–849.e21.

Newman, A.M., Liu, C.L., Green, M.R., Gentles, A.J., Feng, W., Xu, Y., Hoang, C.D., Diehn, M., and Alizadeh, A.A. (2015). Robust enumeration of cell subsets from tissue expression profiles. Nat. Methods *12*, 453–457.

Pillay, J., Tak, T., Kamp, V.M., and Koenderman, L. (2013). Immune suppression by neutrophils and granulocytic myeloid-derived suppressor cells: similarities and differences. Cell. Mol. Life Sci. *70*, 3813–3827.

Powell, D.R., and Huttenlocher, A. (2016). Neutrophils in the Tumor Microenvironment. Trends Immunol. *37*, 41–52.

Quail, D.F., and Joyce, J.A. (2017). The Microenvironmental Landscape of Brain Tumors. Cancer Cell *31*, 326–341.

Robinson, M.D., McCarthy, D.J., and Smyth, G.K. (2010). edgeR: a Bioconductor package for differential expression analysis of digital gene expression data. Bioinformatics *26*, 139–140.

Rodriguez, P.C., Quiceno, D.G., Zabaleta, J., Ortiz, B., Zea, A.H., Piazuelo, M.B., Delgado, A., Correa, P., Brayer, J., Sotomayor, E.M., et al. (2004). Arginase I production in the tumor microenvironment by mature myeloid cells inhibits T-cell receptor expression and antigen-specific T-cell responses. Cancer Res. *64*, 5839–5849.

Sagiv, J.Y., Michaeli, J., Assi, S., Mishalian, I., Kisos, H., Levy, L., Damti, P., Lumbroso, D., Polyansky, L., Sionov, R.V., et al. (2015). Phenotypic diversity and plasticity in circulating neutrophil subpopulations in cancer. Cell Rep. *10*, 562–573.

Sedgwick, J.D., Schwender, S., Imrich, H., Dörries, R., Butcher, G.W., and ter Meulen, V. (1991). Isolation and direct characterization of resident microglial cells from the normal and inflamed central nervous system. Proc. Natl. Acad. Sci. USA *88*, 7438–7442.

Shaul, M.E., and Fridlender, Z.G. (2019). Tumour-associated neutrophils in patients with cancer. Nat. Rev. Clin. Oncol. *16*, 601–620.

Shen, M., Hu, P., Donskov, F., Wang, G., Liu, Q., and Du, J. (2014). Tumor-associated neutrophils as a new prognostic factor in cancer: a systematic review and meta-analysis. PLoS ONE *9*, e98259.

Soda, Y., Marumoto, T., Friedmann-Morvinski, D., Soda, M., Liu, F., Michiue, H., Pastorino, S., Yang, M., Hoffman, R.M., Kesari, S., and Verma, I.M. (2011). Transdifferentiation of glioblastoma cells into vascular endothelial cells. Proc. Natl. Acad. Sci. USA *108*, 4274–4280.

Sørensen, M.D., Dahlrot, R.H., Boldt, H.B., Hansen, S., and Kristensen, B.W. (2018). Tumour-associated microglia/macrophages predict poor prognosis in high-grade gliomas and correlate with an aggressive tumour subtype. Neuropathol. Appl. Neurobiol. *44*, 185–206.

Swamydas, M., and Lionakis, M.S. (2013). Isolation, purification and labeling of mouse bone marrow neutrophils for functional studies and adoptive transfer experiments. J. Vis. Exp., e50586.

Templeton, A.J., McNamara, M.G., Šeruga, B., Vera-Badillo, F.E., Aneja, P., Ocaña, A., Leibowitz-Amit, R., Sonpavde, G., Knox, J.J., Tran, B., et al. (2014). Prognostic role of neutrophil-to-lymphocyte ratio in solid tumors: a systematic review and meta-analysis. J. Natl. Cancer Inst. *106*, dju124.

Uribe-Querol, E., and Rosales, C. (2015). Neutrophils in Cancer: Two Sides of the Same Coin. J. Immunol. Res. *2015*, 983698.

Veglia, F., Sanseviero, E., and Gabrilovich, D.I. (2021). Myeloid-derived suppressor cells in the era of increasing myeloid cell diversity. Nat. Rev. Immunol., 1–14.

Verhaak, R.G., Hoadley, K.A., Purdom, E., Wang, V., Qi, Y., Wilkerson, M.D., Miller, C.R., Ding, L., Golub, T., Mesirov, J.P., et al.; Cancer Genome Atlas Research Network (2010). Integrated genomic analysis identifies clinically relevant subtypes of glioblastoma characterized by abnormalities in PDGFRA, IDH1, EGFR, and NF1. Cancer Cell *17*, 98–110.

Wang, Q., Hu, B., Hu, X., Kim, H., Squatrito, M., Scarpace, L., deCarvalho, A.C., Lyu, S., Li, P., Li, Y., et al. (2017). Tumor Evolution of Glioma-Intrinsic Gene Expression Subtypes Associates with Immunological Changes in the Microenvironment. Cancer Cell *32*, 42–56.e6.

Wiencke, J.K., Koestler, D.C., Salas, L.A., Wiemels, J.L., Roy, R.P., Hansen, H.M., Rice, T., McCoy, L.S., Bracci, P.M., Molinaro, A.M., et al. (2017). Immunomethylomic approach to explore the blood neutrophil lymphocyte ratio (NLR) in glioma survival. Clin. Epigenetics *9*, 10.

CellPress
OPEN ACCESS

STAR★METHODS

KEY RESOURCES TABLE

REAGENT or RESOURCE	SOURCE	IDENTIFIER
Antibodies		
Rat Anti-mouse CD45-FITC (Clone I3/2.3)	Biolegend	Cat# 147709; RRID: AB_2563541
Rat Anti-mouse CD11b-BV785 (Clone M1/70)	Biolegend	Cat# 101243;RRID: AB_2561373
Armenian hamster Anti-mouse CD11c-BV605 (Clone N418)	Biolegend	Cat# 117333; RRID:AB_11204262
Rat Anti-mouse Ly-6C-APC (Clone HK1.4)	Biolegend	Cat# 128015; RRID:AB_1732087
Rat Anti-mouse Ly-6G-PE (Clone 1A8)	Biolegend	Cat# 127607;RRID: AB_11204262
Rat Anti-mouse CD3-APC (Clone 17A2)	Biolegend	Cat# 100236; RRID: AB_2561455
Rat Anti-mouse CD4-BV785(Clone GK1.5)	Biolegend	Cat# 100453;RRID: AB_2565843
Rat Anti-mouse CD8-FITC (Clone 53-6.7)	Biolegend	Cat# 100726;RRID: AB_312744
Rat Anti-mouse Ly-6G/Ly-6C(Gr-1)-PE (Clone RB6-8C5)	Biolegend	Cat# 108407;RRID: AB_313366
Rabbit anti-mouse fibronectin	Abcam	Cat# ab2413;RRID: AB_562115
Rabbit anti-mouse Olig2	Millipore	Cat # AB9610;RRID: AB_10807410
Rabbit anti-mouse vWF	Abcam	Cat # AB6994;RRID: AB_2890983
Rabbit anti-mouse Iba1	Wako	Cat# 019-19741; RRID: AB_839504
Rabbit anti-mouse CD68	Bio-Rad	Cat# MCA1957GA; RRID: AB_324217
Rabbit anti-mouse GFAP	Sigma	Cat#SAB5700611; RRID: AB_2827276
Chicken anti-mouse nestin	Abcam	Cat # ab134017; RRID: AB_2753197
Rabbit anti mouse-Ki67	Cell signaling	Cat #12202; RRID: AB_2620142
Rat anti-mouse LY6G (Clone 1A8,InVivoMAb)	Bio-X-Cell	Cat# BE0075-1; RRID: AB_1107721
Rat anti-mouse IgG2a (Clone 2A3,InVivoMAb)	Bio-X-Cell	Cat# BE0089; RRID: AB_1107769
Anti-mouse CD3 (Clone 145-2C11)	Biolegend	Cat#100331; RRID:AB_1877073
Anti-mouse CD28 (Clone 37.51)	Biolegend	Cat# 102112; RRID:AB_312877
Alexa 647 Goat anti-Rabbit IgG	Abcam	Cat # AB150079; RRID: AB_2722623
Alexa 647 Donkey anti-Rat IgG	Biolegend	Cat# 407511; RRID: AB_2716139
Chemicals, peptides, and recombinant proteins		
Recombinant human EGF	Promega	Cat# 9PIG502
Recombinant human basic FGF	Peprotech	Cat# 100-18C
Recombinant IL-2	Peprotech	Cat# 200-02
N2 Supplement	GIBCO	Cat# 17502048
D-Luciferin Firefly	GoldBio	Cat# Luck-250
DAPI	Biolegend	Cat# 422801
Trizol	Bio Labs Ltd.	Cat# 009010233100
Histopaque-1077	Sigma-Life Sciences	Cat# 10771
Histopaque-1199	Sigma-Life Sciences	Cat# 11991
Critical commercial assays		
Neural dissociation kit	Miltenyi Biotec	Cat# 130-092-628
qScript cDNA Synthesis kit	Quantas bio	Cat# 95047-100
TruSeq RNA library prep kit	Illumina	Cat# RS-122-2001
RNeasy Mini Kit	QIAGEN	Cat# 74104
Deposited data		
RNaseq data MES versus PN tumors	This paper	GEO: GSE73127
RNaseq data naive versus educated neutrophils	This paper	GEO: GSE169286

(*Continued on next page*)

Continued

REAGENT or RESOURCE	SOURCE	IDENTIFIER
Experimental models: Cell lines		
Mouse: R53-GSCs	This paper	N/A
Mouse: R53-DGCs	This paper	N/A
Mouse: PD53-GSCs	This paper	N/A
Experimental models: Organisms/strains		
FVB-Tg(GFAP-cre)25Mes/J mice	The Jackson Laboratory	Cat# JAX:004600; RRID:IMSR_JAX:004600
B6.Cg-Tg(Syn1-cre)671Jxm/J mice	The Jackson Laboratory	Cat# JAX:003966; RRID:IMSR_JAX:003966
C57BL/6J mice	Envigo, Israel	N/A
Oligonucleotides		
See Table S1	This paper	N/A
Recombinant DNA		
pTomoHRas-shp53	Friedmann-Morvinski et al., 2012	N/A
pTomoPDGFB-shp53	This paper	N/A
pTomo-mock	Marumoto et al., 2009	RRID:Addgene_26291
Software and algorithms		
ImageJ (FIJI version 2.0)	NIH and LOCI, University of Wisconsin	https://imagej.nih.gov/ij/; RRID: SCR_00285
Graphpad Prism Version 8.2.1	GraphPad Software, La Jolla California USA	https://www.graphpad.com:443/; RRID: SCR_002798
BioRender	Information Technology Company, Toronto, Ontario	https://biorender.com/; RRID: SCR_018361
CIBERSORT	Newman et al., 2015	https://cibersort.stanford.edu/; RRID: SCR_016955

RESOURCE AVAILABILITY

Lead contact

Further information and requests for resources and reagents should be directed to and will be fulfilled by the Lead Contact, Dinorah Friedmann-Morvinski (dino@tauex.tau.ac.il)

Materials availability

All plasmids and murine cell lines generated in this study can be obtained following establishment of a Material Transfer Agreement.

Data and code availability

- The RNaseq data generated during this study are available at GEO: GSE73127 and GEO: GSE169286.
- This paper does not report original code.
- Any additional information required to reanalyze the data reported in this paper is available from the lead contact upon request.

EXPERIMENTAL MODEL AND SUBJECT DETAILS

Animals and ethics statement

hGFAP-Cre and SynapsinI-Cre transgenic mice were all purchased from the Jackson Laboratories. C57BL/6J female mice were purchased from Envigo Jerusalem Israel. All experiments involving animals were approved by the Tel Aviv University Institutional Animal Care and Use Committee. All mice, females and males used in this study were 8-16 weeks old when tumors were induced, and bred under pathogen-free conditions. All animals were housed in individually ventilated cages (5 mice per cage) with autoclaved ASPEN wood chips bedding, and provided with food and drinking water *ad libitum* with 12/12-hour light/dark cycle. Animal experiments were approved by the animal care and use committee (IACUC) of Tel Aviv University (approval protocol no. 04-19-074) and conducted in accordance with NIH guidelines.

Cell culture

PD53-GSC and R53-GSC lines were generated by tissue dissociation of tumors induced by lentiviral injections of PDGFB-shp53 and HRas-shp53 lentivirus in GFAP-Cre or SynapsinI-Cre mice, respectively. Cells were cultured in stem cell media: DMEM-F12 (Biological Industries-BI) containing 1% Penicillin/Sreptomycin (BI), 1% Glutamax (BI), N2 supplement (GIBCO), 50 μg/ml Heparin (Sigma-Aldrich) 20 ng/ml rhEGF (Promega) and 20 ng/ml recombinant-hFGF (Peprotech). PD53-GSC and R53-GSC murine lines generated in this study were not authenticated.

METHOD DETAILS

Stereotaxic injections

HRas-shp53 (Friedmann-Morvinski et al., 2012) lentivirus (10^9/ml IU in 1 μL of Hank's Balanced Salt Solution, without Ca^{2+}, Mg^{2+}, HBSS) was stereotaxically injected in the cortex (CTX; AP = −2.0, ML = −1.5, DV = 1.0) of both male and female SynapsinI-Cre transgenic mice. PDGFB-shp53 lentivirus (10^9/ml IU in 1ul) was stereotaxically injected in the subventricular zone (SVZ; AP = −1.5, ML = −2.0, DV = 2.3) of both male and female transgenic GFAP-Cre mice. Syngeneic R53 and PD53 glioma models were generated by dissociating lentiviral-induced tumors and low passage murine-derived tumor cells ($3x10^5$ GSCs in 1.5 μL of HBSS) were orthotopically injected in the hippocampus (HP; AP = −2.0, ML = −1.5, DV = 2.3) of C57BL/6 female mice. Mice were anesthetized by isoflurane and placed in a Kopf Sterotaxic Alignment System and injected as previously described (Friedmann-Morvinski and Singer, 2013). Two weeks post intracranial injections, mice were randomly assigned to treated and vehicle (control) group. The treated mice received 200 μL (25mg/kg) of TMZ by oral gavage for 10 days.

Quantitative real-time PCR (qRT-PCR) analysis

Total RNA was isolated using Trizol (Bio Labs Ltd.). Tumors were homogenized in 1ml of Trizol utilizing a pellet pestle. Reverse transcription was performed with qScript (95047-100, Quanta Biosciences) in all experiments. qRT-PCR reactions were carried out with the StepOnePlus Real Time-PCR System (AB Applied Biosciences) using SYBR Green Realtime PCR Master Mix (ThermoFisher). Data are presented after normalization with cyclophilin. The primers are listed in Table S1.

Flow cytometry and immunofluorescence staining

Brain tumors (GFP+ tissue resected under fluorescent microscope) were dissociated using a neural dissociation kit (Miltenyi Biotec) according to manufacturer's instructions and the resulting cell suspension was cleaned of debris (myelin) via Percoll (P4937-500ML, Sigma-Aldrich) density gradient centrifugation at 950x*g* for 20 min at 4°C without deceleration. CD45+ cells were enriched using anti-CD45 magnetic-microbead and MS columns (Miltenyi Biotec) according to manufacturer's instructions. The enriched cells were first fixed and stained for live-cell population with eflour-405 Live/Dead Fixable dye (eBiosciences) and then incubated with TruStain FcX™-Fc blocker CD16/32 (Biolegend). Following blocking, the samples were stained with different combinations of anti-mouse antibodies listed in Key Resources Table for 30min at 4°C in the dark. Cells were washed and resuspended in PBS prior to acquisition on Attune NxT Flow Cytometer and analysis was performed using Kaluza software v2.1.

For confocal fluorescence imaging analysis, mice were perfused transcardially with 1x PBS and fixed with 4% paraformaldehyde (PFA). The brains were further fixed in cold PFA overnight at 4°C, washed with PBS and dehydrated with 30% sucrose in PBS. Coronal sections (30-40 μm) were cut using a HM450 Microtome (ThermoFisher Scientific). For staining, floating sections were permeabilized with 0.25% Triton X-100 and then blocked with 3% normal goat serum with 0.25% Triton X-100 for 1 h. Primary antibodies listed in Key resources table were diluted in 0.3% normal goat serum with 0.25% Triton X-100 and incubated with brain sections overnight at 4°C in a humidified chamber. The next day, sections were washed with PBS and secondary antibodies were incubated for 1 hr at room temperature (RT). After three washes with PBS, sections were incubated with DAPI for 5 min at RT, washed again, and mounted with Fluoromount-G® (SouthernBiotech). Images were obtained using a Zeiss LSM 800 Confocal Microscope.

Neutrophil depletion and Bioluminescence Imaging

For neutrophil depletion mice were administered intraperitoneally (i.p.) with 200 μg of either rat anti-LY6G (clone 1A8, Bio-X-Cell) or rat anti-IgG2a (Bio-X-Cell) isotype control every alternate day for 2 weeks as indicated in Figure 4C. Neutrophils depletion was monitored by flow cytometry analysis of blood samples using Ly-6G/Ly-6C (Gr-1)-PE and CD11b-BV785. Antibodies listed in Key resources table. Mice bearing luciferase-expressing tumors received injections of 3 mg per mouse i.p. of D-Luciferin Firefly (GoldBio; #Luck-250). The mice were then anesthetized and imaged using a PhotonImager™ (BioSpace Labs) system, 10 min after i.p. injection of luciferin.

Modified Winn assay

A mixture of either $3x10^5$ nNΦ with $3x10^5$ R53-GSC-luc or eNΦ with $3x10^5$ R53-GSC-luc (ratio 1:1) was stereotaxically injected into the brain of C57BL/6 female mice. R53-GSC-luc ($3x10^5$ cells 1:1 in PBS) were injected as control. Bioluminescence live imaging was performed twice a week to monitor tumor growth.

Isolation of Bone marrow derived Neutrophils and functional analysis

Bone marrow derived neutrophils were isolated from either tumor free wild-type mice (nNΦ) or mice bearing R53-GSC tumors (eNΦ), by gradient centrifugation, as previously described (Swamydas and Lionakis, 2013). Briefly, bone marrow (BM) cells were collected by flushing the bones of the hind limbs with RPMI-1640, 1% Penicillin/Streptomycin, 1% Glutamax, 0.5% FBS and 2mM EDTA. Following red blood cells lysis, the BM cells were resuspended in 1mL of ice-cold PBS and layered on top of a pre-layered solution of 3 mL Histopaque-1077 (Sigma-Life Sciences #10771) on top and 3 mL Histopaque-1199 (Sigma-Life Sciences #11191) on the bottom and centrifuged at 2000 rpm for 30 min without brake. Neutrophils were collected from the lower interface, washed and counted.

Neutrophil migration assay

Either nNΦ or eNΦ ($2x10^5$ cells/well) were applied to the top chamber of a 3 μm Transwell inserts (Millicell). The bottom chamber of the 24-well plate was filled with 800 μL of R53-GSC conditioned media (CM), the plate was then incubated overnight at 37°C and 5% CO_2. Experiments were run in duplicates. At the end of the incubation, the top chamber was removed and the number of neutrophils that have migrated to the bottom chamber was counted.

Neutrophil cytotoxic effect

R53-GSCs expressing luciferase were co-culture with either nNΦ or eNΦ at the indicated E:T ratios. The R53-GSCs were also incubated in media without neutrophils as control. The plate was incubated overnight at 37°C and 5% CO_2. The following day, 10 μL of D-Luciferin firefly (15mg/ml) was added to the wells and images were taken in a PhotonImager™ (BioSpace Labs) system and analyzed using M3 vision software. The cell-mediated-cytotoxicity was calculated using the formula: 1- [(Luminescence of R53-GSC with neutrophils)/ (Luminescence of R53-GSC in medium)] X 100.

Neutrophil production of Reactive Oxygen Species (ROS)

H_2O_2 production was detected in unstimulated cells or by stimulating freshly isolated nNΦ or eNΦ with 10nM Phorbol 12-myristate 13-acetate (PMA). Chemiluminescence was measured at 430 nm immediately after adding 500uM Luminol (Sigma-Aldrich) for 30 min at 1 min intervals, using a plate-reader (Synergy HT micro plate reader, BioTek).

NETosis

Freshly isolated nNΦ or eNΦ were plated on coverslip coated with poly-L-Lysine and exposed to glioma CM overnight, fixed with 4% PFA, stained for DAPI and imaged using a Zeiss LSM 800 Confocal Microscope.

Suppression of T cell proliferation by neutrophils

Splenocytes were isolated from the spleen of a euthanized naive C57BL/6 mouse. Following red blood cell lysis, $1x10^7$ splenocytes were labeled with Celltrace™ Violet (Thermo Fisher) and cultured in stimulation media containing soluble antiCD3 and antiCD28 antibodies (30 ng/mL each, BioLegend) and 100 U/mL of IL-2 for 3 days ($1x10^6$ labeled cells in 300 μl/well in a 24-well plate). To assess suppression of T cell proliferation, either nNΦ or eNΦ (1:1 ratio) were added to the CellTrace labeled splenocytes (to a final volume of 500 μl) and incubated in the same stimulation media for 72 hr. The cells were collected, stained with CD3-APC antibody and analyzed by FACS to follow CellTrace dilution using an Attune NxT Flow Cytometer.

Morphology of neutrophils

Following bone marrow isolation, nNΦ or eNΦ were resuspended at a concentration of $5x10^4$ cells/ml, and 100 μL were centrifuged at 1000 rpm, 5 min at RT in a Shandon cytospin (Thermo Fisher Scientific). The neutrophils on the slides were fixed and stained with hematoxylin and eosin using Hemacolor Rapid Staining kit (Merk). Samples were then mounted and images were taken under a light microscope.

Tube formation assay

005 GSCs glioma cells ($1x10^6$) were first incubated in EGM-2 media (Lonza) with 100 μg/mL of DFO mesylate (Sigma) to reproduce hypoxic conditions for 72 hr (Soda et al., 2011). The obtained tumor derived endothelial cells (TDECs; $1x10^5$ cells) were then seeded on Matrigel together with either nNΦ or eNΦ (1:1) and incubated at 37°C, 5% CO_2 for 4 hr. Images were taken using an epiflouroscent microscope (Nikon Eclipse Ti).

RNaseq analysis: Neutrophils

RNA was isolated from bone marrow derived neutrophils using RNeasy Mini Kit (QIAGEN). The integrity of RNA was assessed using Agilent Tape station 2200 and samples with RIN > 7.0 were used. Libraries were constructed using TruSeq RNA library prep kit (Illumins) following manufacturer protocols. RNA sequencing was performed using an Illumina NextSeq500, 75bp configuration and ≥ 400 million raw single-end reads. An average of 23.8 million reads per sample were sequenced across 8 samples. Trimming was performed on low-quality reads. Alignment was performed using STAR - 2.6.1d and quantified to mm10 using Ensemble transcript release 95. The RNA-sequencing reads were converted to transcriptome abundant matrix in the format of RPKM (Reads Per Kilobase Million). Differential gene expression was performed using Partek Flow (10.0.21.0411) GSA (Gene Specific Analysis) and

differentially expressed genes were obtained using cutoff p [FDR] < 0.05 and fold-change difference 1.5. Heatmaps were performed using Partek Genomics Suite (7.19.1125). Database for Annotation, Visualization and Integrated Discovery (DAVID) functional enrichment tool v6.8 was used for function and pathway annotation (Huang et al., 2009).

RNaseq analysis: Tumors

At end point, brains were collected and normal brain tissue was trimmed away from GFP+ tumor tissue under a dissecting fluorescent microscope. RNA was isolated using the RNeasy kit (QIAGEN), cDNA libraries were prepared using the TruSeq stranded mRNA kit (Illumina), and the sequencing was performed using a NovaSeq Sequencing System (Illumina). Raw sequence data (30 million reads average per sample) was trimmed using fastp 0.20.1 (Chen et al., 2018) and aligned to the GRCm38 assembly using STAR 2.7.2a (Dobin et al., 2013). Count data was normalized using DESeq2 1.30.1 (Love et al., 2014) and heatmaps were made with ComplexHeatmap 2.6.2 (Gu et al., 2016) after gene-wise Z-scoring.

TCGA dataset processing and Gene Set Enrichment Analysis (GSEA)

The RNA-seq data was downloaded from the TCGA database, the selected samples were all patient tissue samples. All the cancer tissues and normal tissues were compared using R package *edgeR* v3.13 (McCarthy et al., 2012; Robinson et al., 2010). An average raw read counts of < 1 were removed prior to DEGs calculation. The expression Fold change was calculated between tumor and normal group. FDR < 0.05|logFC| > 0.58 were set as inclusion criteria for DEGs. GSEA was carried out using the GSEA software, version 4.0.3, obtained from the Broad Institute. Expression datasets (.GCT format), phenotype labels (.CLS format) and annotations (.CHIP format) were created according to GSEA specifications. Gene set analysis was performed using gene sets from the Molecular Signatures Database (MSigDB v5.2 downloaded from http://bioinf.wehi.edu.au/software/MSigDB/). We computed overlaps using C7 (immunologic gene set) collection (Hay SB Experimental hematology 2018). Transcriptomic data of glioma were extracted from the TCGA database and NBT data was acquired from healthy donors in Alzheimer's study (GEO dataset E-GEOD36980 was downloaded and data of only reference control samples were used).

Gene ontology (GO) analysis

Statistically overrepresented GO categories within top ranked differentially expressed gene lists were determined using DAVID Functional Annotation Bioinformatics Microarray Analysis (Ashburner et al., 2000). The statistical test was the Hypergeometric test with Benjamini & Hochberg False Discovery Rate (FDR) correction and 0.05 significance level. GO annotation and ontology files were from the GO consortium (http://geneontology.org/),

QUANTIFICATION AND STATISTICAL ANALYSIS

Statistical analysis and graphing were performed using GraphPad Prism version 8.2.1. Log-rank analysis was used to determine statistical significance of Kaplan-Meier survival plots. All *in vitro* and *ex-vivo* experiments were repeated at least 3 times, and all animal studies were carried out twice with at least 3-5 animals in each group for the FACS analysis and 5-6 mice for the depletion and Winn assay. Data represents Mean ± SEM. P value of < 0.05 were considered significant. Information on biological and technical replicates and the statistical tests used are included in figure legends.

Cell Reports, Volume *36*

Supplemental information

Exploring the longitudinal glioma microenvironment landscape uncovers reprogrammed pro-tumorigenic neutrophils in the bone marrow

Prerna Magod, Ignacio Mastandrea, Liat Rousso-Noori, Lilach Agemy, Guy Shapira, Noam Shomron, and Dinorah Friedmann-Morvinski

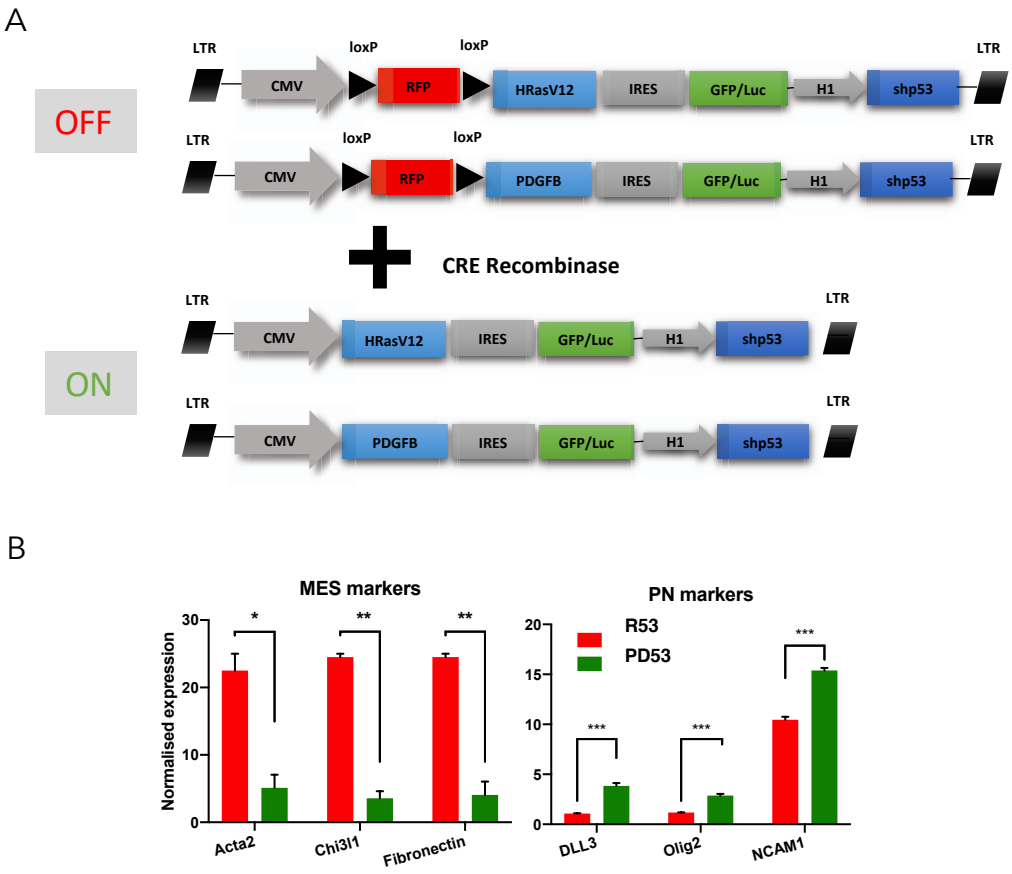

Fig S1 related to Fig 1. Generation and characterization of R53 and PD53 murine GBM models. A. Schematic representation of the lentiviral vector. The upper schemes show the pTomo lentiviral vector constructs with HRasV12 (Friedmann-Morvinski et al., 2012) or PDGFB oncogenes under CMV promoter and the lower schemes show the 'active' form of the vector. In the 'Off" state the floxed RFP fragment prevents expression of the oncogene. Only in the presence of Cre recombinase, the floxed RFP cassette is cut out resulting in the expression of the respective oncogenes ('On" state). The shRNA under the H1 promoter targets p53 expression. **B**. RT-qPCR analysis of mRNA levels in R53 and PD53 GBM tumors (n=5). The indicated representative MES and PN markers were analyzed. Gene expression was normalized to cyclophilin expression levels. p value of <0.05 was considered significant, (*) $p<0.05$, (**) $p<0.01$, (***) $p<0.001$.

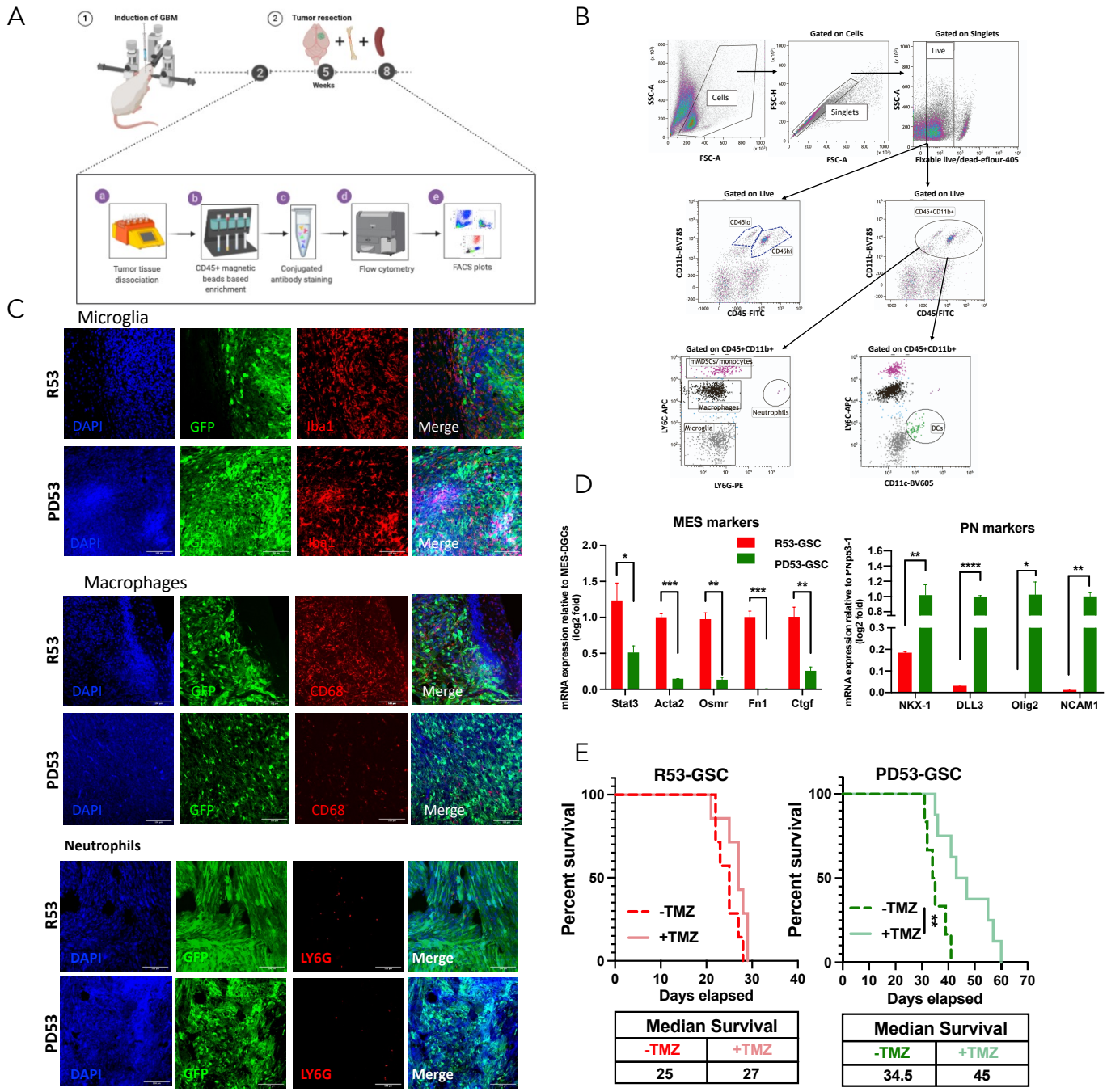

Fig S2 related to Fig 2. Immune cell microenvironment analysis in R53 and PD53 GBM models. A, Schematic representation of the workflow for FACS analysis of tumor microenvironment. The transgenic mice were injected with lentiviral vectors using a stereotactic instrument. At 2, 5 weeks or at the end of the disease (approx. 8 weeks) the mice were sacrificed, the brain, hind limbs and spleen were harvested. The tumor was resected using GFP as a guide to determine tumor borders and the bone-marrow was flushed for isolating cells. The tumor was dissociated to single cells and CD45+ cells were enriched using magnetic separation (Miltenyi). Next, cells (from tumor, bone marrow and spleen) were stained with the antibodies in listed in Key Resource Table and then analysed by flow cytometry. B, Representative flow cytometric gating strategy: the cells were all gated on live cells and singlets and then on CD45-FITC and CD11b-BV785, the CD45 and CD11b positive cells were then plotted against LY6C-APC and LY6G-PE-the immune cell population are depicted by the respective colors, for DCs the CD45+CD11b+ cells were plotted against CD11c-BV605 and the population positive for CD11c was considered. (MDSC-myeloid derived suppressor cells, DCs-Dendritic cells). C. Representative immunofluorescence images of R53 and PD53 tumor sections stained with Iba1 (microglia marker), CD68 (macrophage marker) and LY6G (neutrophil marker). DAPI was used as nuclear marker and GFP is expressed only in tumor cells. Scale bar = 100µm . D. RT-qPCR analysis of mRNA levels in R53-GSCs and PD53-GSCs cells, derived from R53 and PD53 mouse models, respectively (n=3) . Representative MES and PN markers were analyzed. Gene expression was normalized to cyclophilin expression levels. p value of <0.05 was considered significant, (*) p<0.05, (**) p<0.01, (***) p<0.001. E. Kaplan Meyer survival curves for R53-GSCs and PD53-GSCs injected mice either treated (+TMZ) or not treated (-TMZ) with 25 mg/kg in 200 ul of TMZ for 10 days. n=7 per group. p value of <0.05 was considered significant, (*) p<0.05, (**) p<0.01, (***) p<0.001.

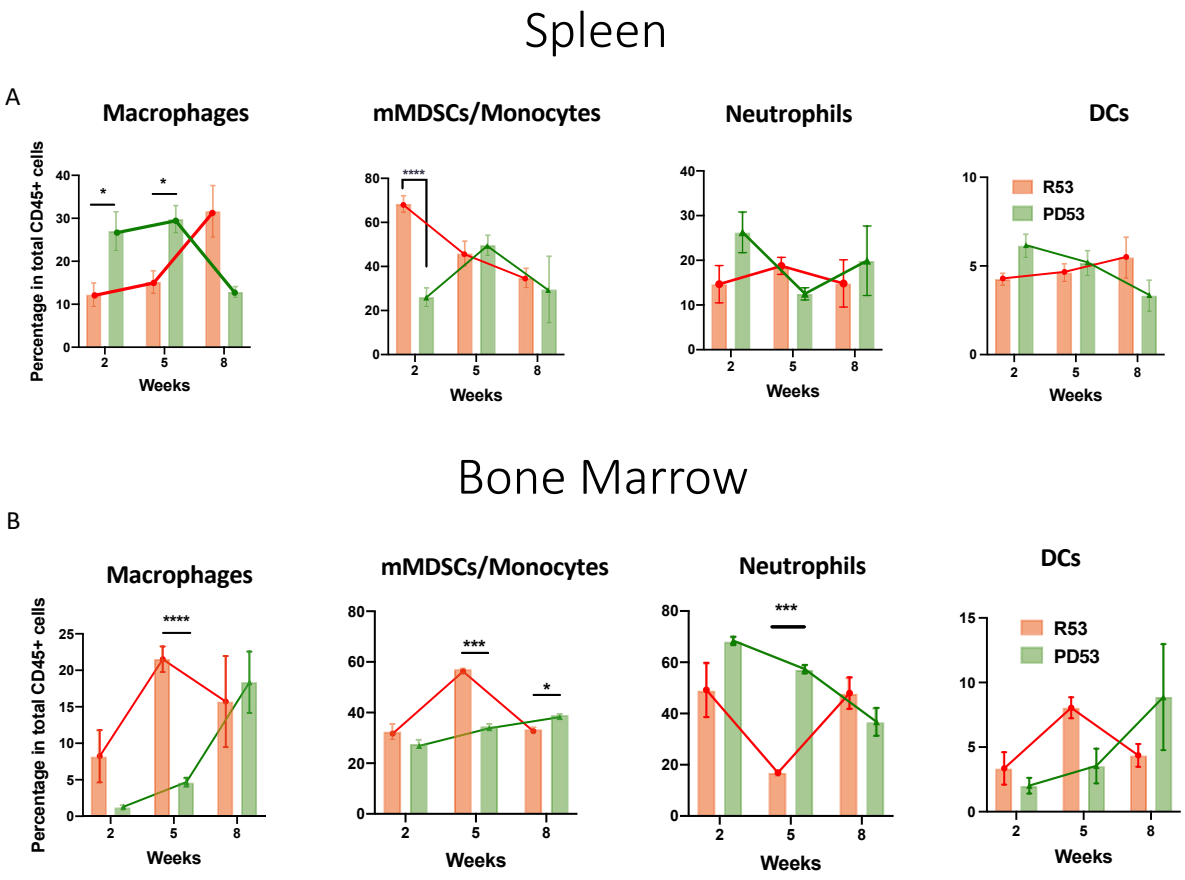

Fig S3 related to Fig2. Immune cell profile analysis at different time points. FACS analyses showing the temporal changes between GBM oncogenic driver models in spleen and bone marrow. All plots are gated on $CD45^{+}CD11b^{+}$ cells. Flow analysis of macrophages, mMDSCs/monocytes, neutrophils and $CD11b^{+}$ DCs among $CD45^{+}$ populations of GBM tumor bearing mice. Mice were euthanized at 2, 5 weeks post intracranial injections or at the end of the disease (approx. 8 weeks); spleen (A) and bone arrow (B) of tumor matched mice were taken for TME analysis. n= 4-5 per group, mean ± SEM, unpaired Student t test. Representative of two independent experiments. p value of <0.05 was considered significant, (*) $p<0.05$, (**) $p<0.01$, (***) $p<0.001$. Not significant values are not mentioned. (mMDSCs-monocytic Myeloid-Derived Suppressor cells, DCs-Dendritic cells)

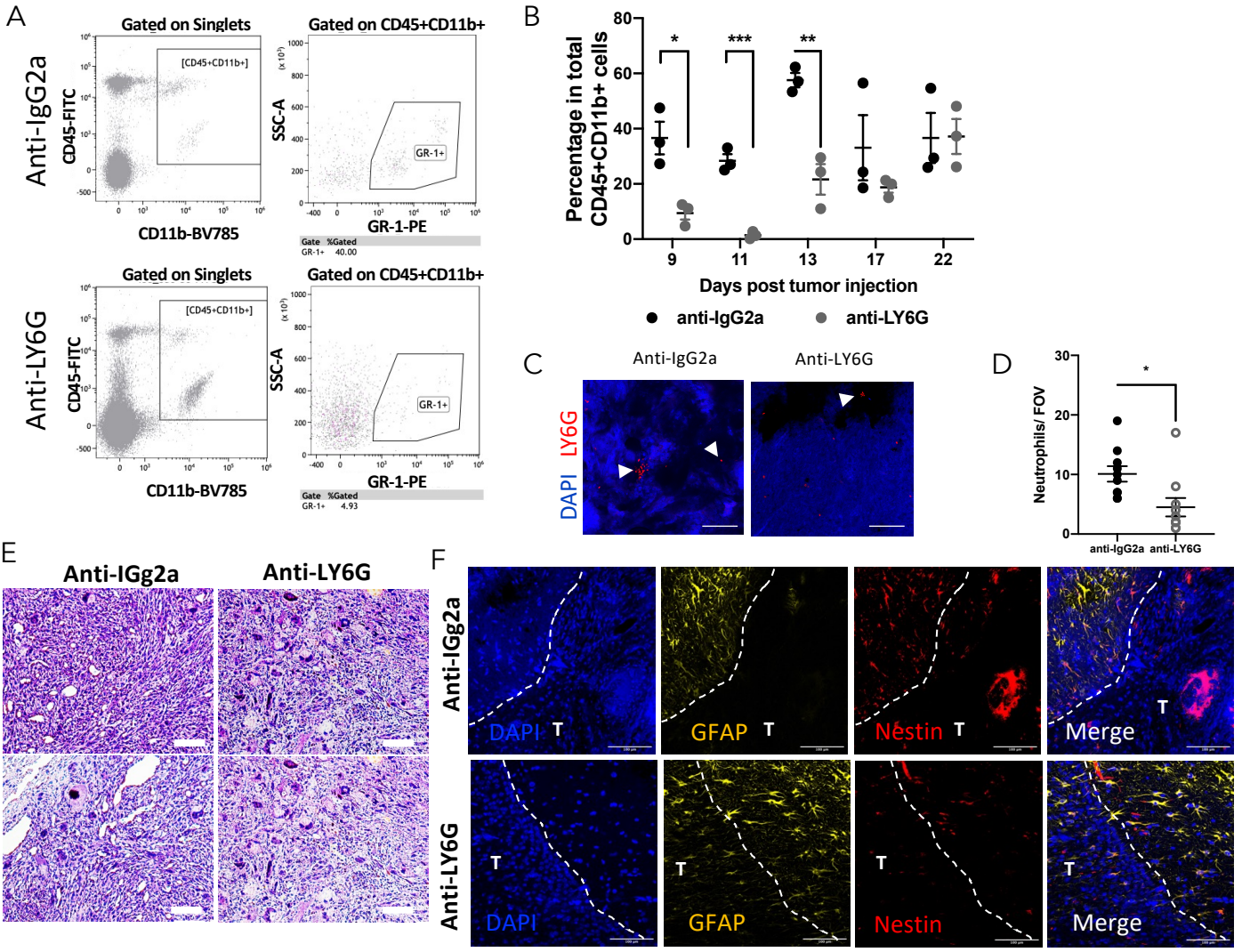

Fig S4 related to Fig 3. Depletion of neutrophils at tumor initiation stage. A, Representative flow cytometry plots showing efficient depletion of neutrophils (GR-1+) in blood of mice treated with an isotype control Ab (anti-IgG2a) or the anti-LY6G specific mAb against neutrophils. B, Graph summarizing the window of efficient neutrophil depletion during isotype control and anti-LY6G treatment. Blood samples were analyzed by flow cytometry at the indicated time points. Mean ± SEM, unpaired Student t-test. n=3 per group. C, Representative confocal microscopy image of isotype control vs neutrophil depleted tumor sections stained with anti-LY6G. D, Quantification of neutrophils per field of view (FOV) in tumor sections of isotype control vs depleted groups of mice at the end of disease progression (quantification of C). Mean ± SEM, unpaired Student t-test. n= 4-5 per group. p value of <0.05 was considered significant, (*) p<0.05, (**) p<0.01, (***) p<0.001. Not significant values are not mentioned. E, Representative Hematoxylin and Eosin (H&E) staining of tumor tissue at endpoint after depletion of neutrophils (GR-1+) in mice treated with an isotype control Ab (anti-IgG2a) or the anti-LY6G specific mAb starting10 days after tumor induction.. F, Immunofluorescent images using GFAP and Nestin markers. G, Immunofluorescent images stained with proliferation marker Ki67 and quantification graph (n=5). Scale bar = 100µm

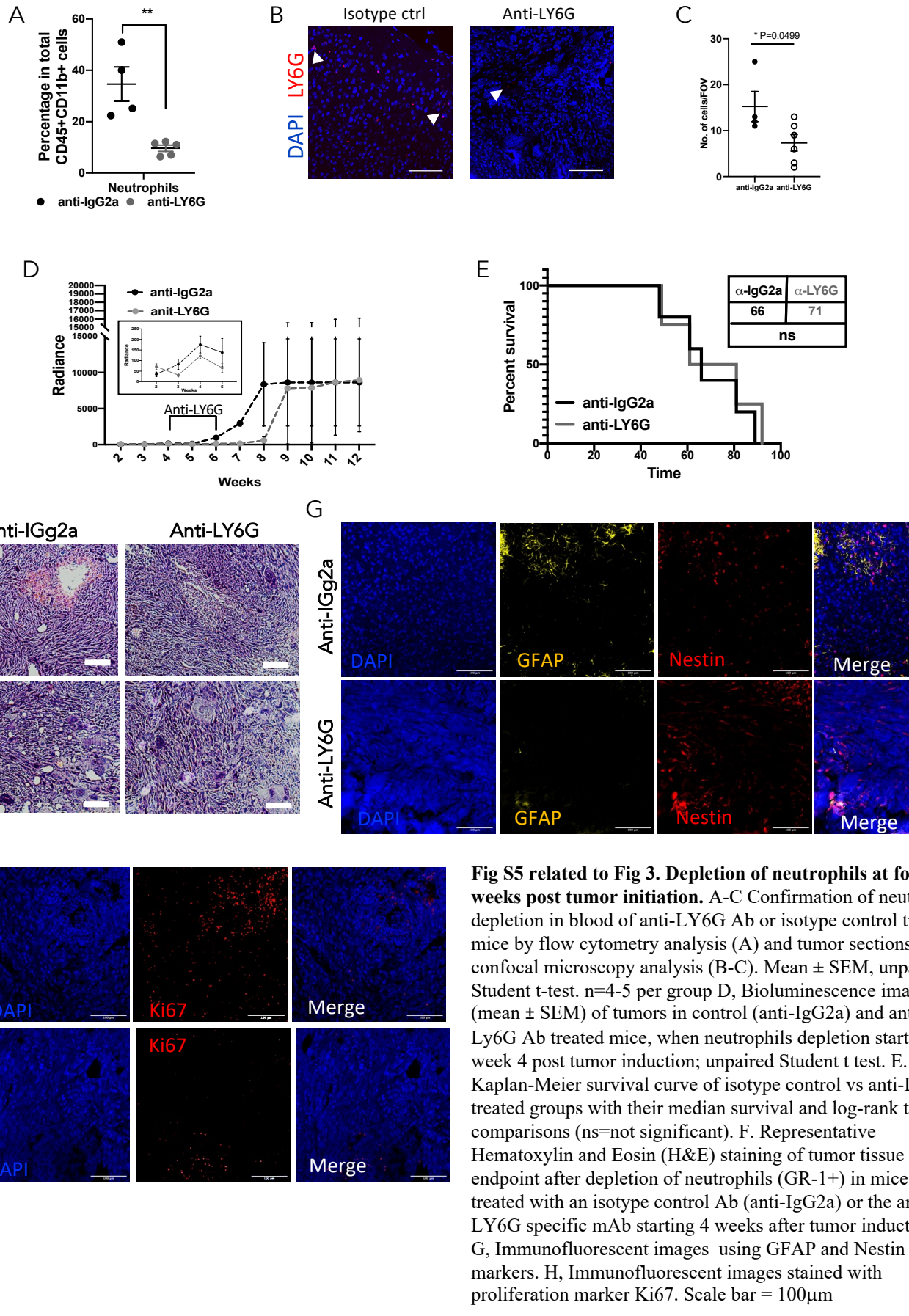

Fig S5 related to Fig 3. Depletion of neutrophils at four weeks post tumor initiation. A-C Confirmation of neutrophil depletion in blood of anti-LY6G Ab or isotype control treated mice by flow cytometry analysis (A) and tumor sections by confocal microscopy analysis (B-C). Mean ± SEM, unpaired Student t-test. n=4-5 per group D, Bioluminescence imaging (mean ± SEM) of tumors in control (anti-IgG2a) and anti-Ly6G Ab treated mice, when neutrophils depletion started at week 4 post tumor induction; unpaired Student t test. E. Kaplan-Meier survival curve of isotype control vs anti-LY6G treated groups with their median survival and log-rank test comparisons (ns=not significant). F. Representative Hematoxylin and Eosin (H&E) staining of tumor tissue at endpoint after depletion of neutrophils (GR-1+) in mice treated with an isotype control Ab (anti-IgG2a) or the anti-LY6G specific mAb starting 4 weeks after tumor induction. G, Immunofluorescent images using GFAP and Nestin markers. H, Immunofluorescent images stained with proliferation marker Ki67. Scale bar = 100µm

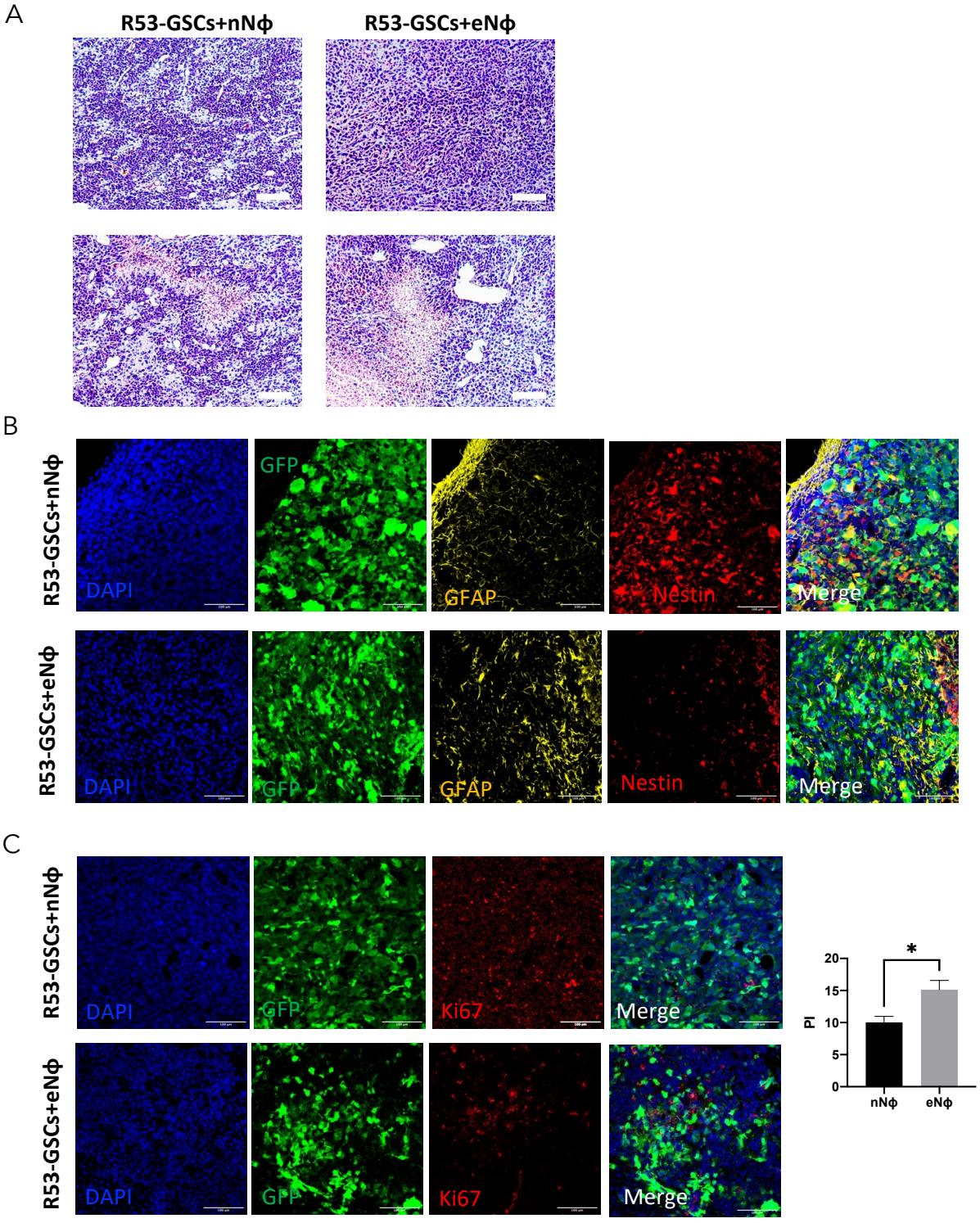

Fig S6 related to Fig 3. Characterization of tumors from WINN assay. A, Representative Hematoxylin and Eosin (H&E) staining of tumor tissue at endpoint of mice co-injected with either R53-GSCs+nNφ or R53-GSCs+eNφ. B, Immunofluorescent staining with GFAP and Nestin markers. C, Immunofluorescent images stained with proliferation marker Ki67 and quantification graph on the right side. Scale bar = 100μm

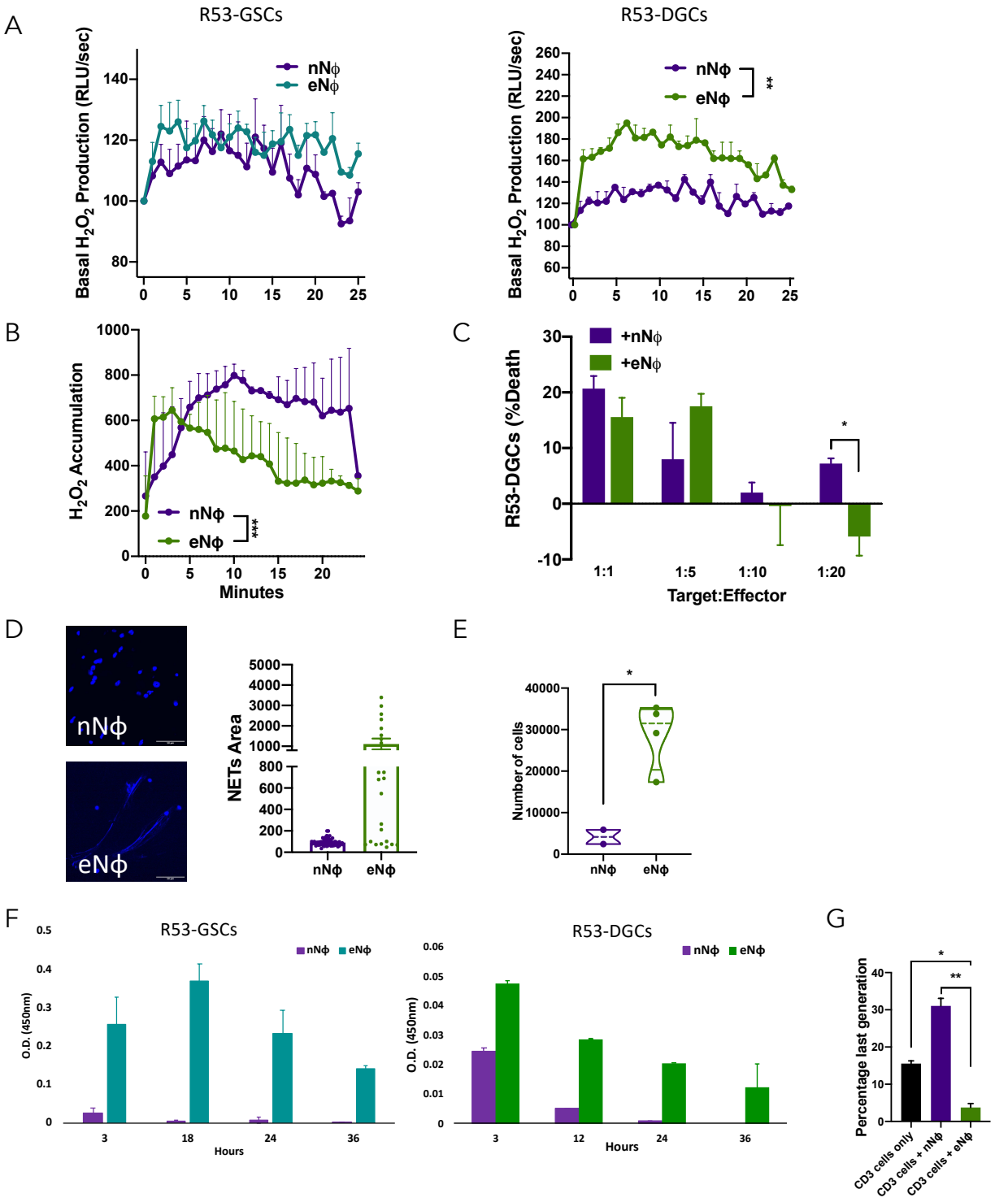

Fig S7 related to Figure 4. Functional characterization of BM derived neutrophils. A Basal H_2O_2 production by unstimulated nNΦ and eNΦ. B, H_2O_2 production by PMA stimulated nNΦ and eNΦ. C, Cytotoxicity effect of nNΦ and eNΦ when co-culture with R53-DGC at the indicated target:effector ratios. D, Representative DAPI-stained (blue) confocal microscopy images of CM induced NETosis in nNΦ and eNΦ. Scale bar = 100 µm. The graph on the right represents the percentage of NET formation (normalized to media control)/ FOV. E, Quantification of the number of migrating neutrophils towards glioma conditioned media. F, WST-1 cell viability assay of cultured nNΦ and eNΦ at the indicated time points. G, *In vitro* T-cell proliferation measured by reduction of cell-tracer dilution assay following co-culture with either nNϕ or eNϕ (1:1). Graph represents quantification of percentage of T cells in the last generation. Mean ± SEM, unpaired Student t test. All experiments were repeated 3 times and performed on neutrophils from naïve and R53-DGCs glioma bearing mice separately. p value of <0.05 was considered significant, (*) p<0.05, (**) p<0.01, (***) p<0.001.

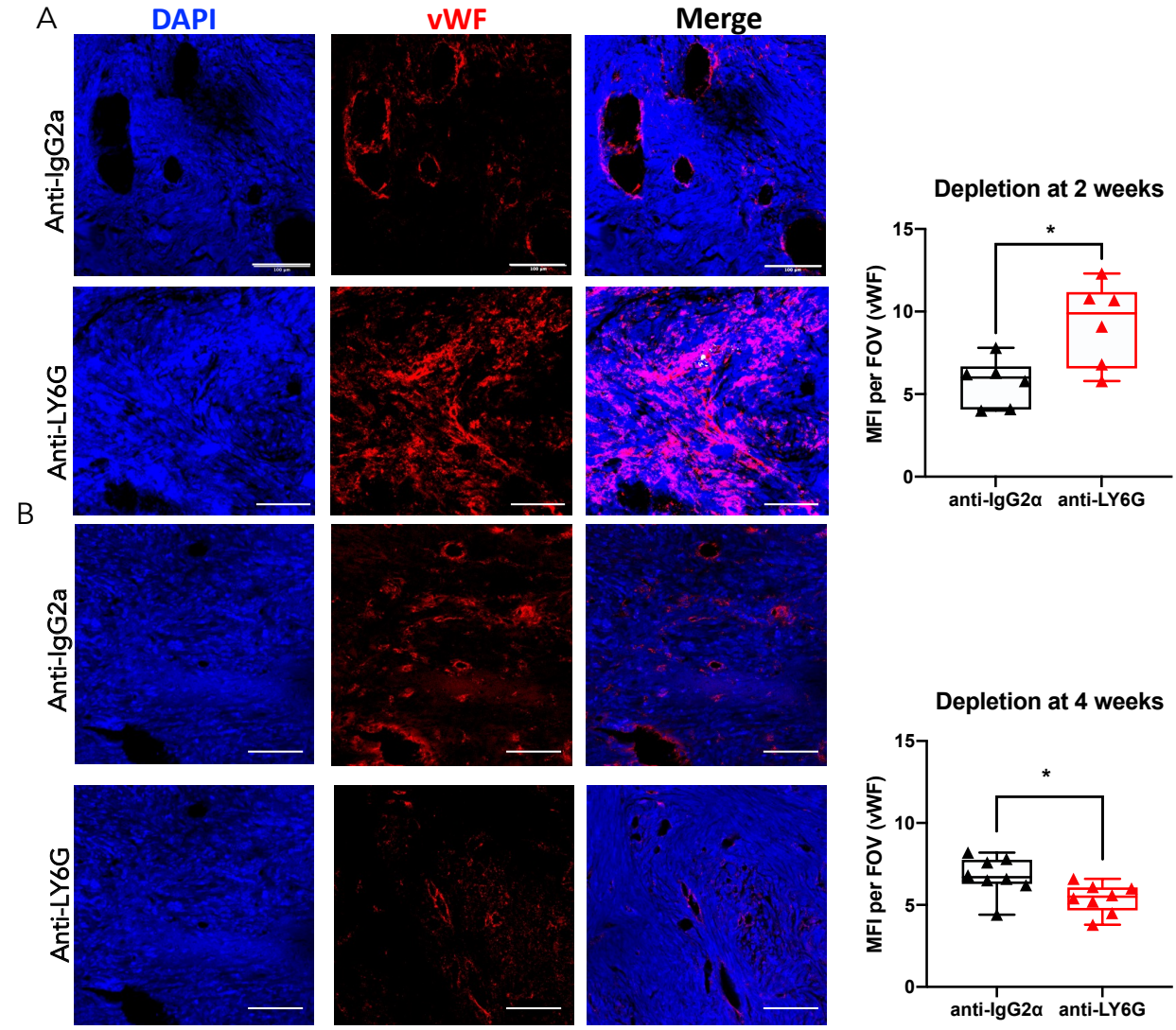

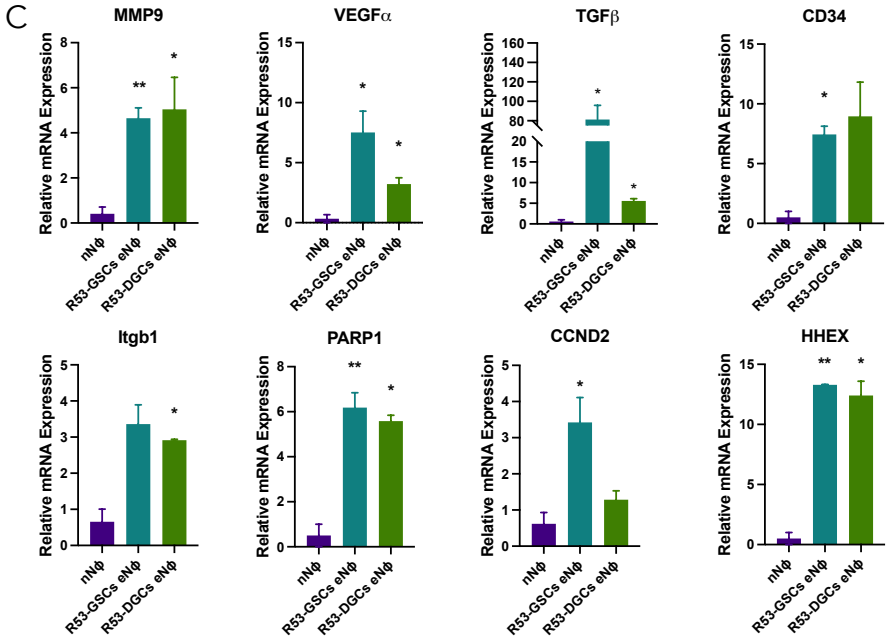

Fig S8 related to Fig 5. Characterization of pro-angiogenic properties of eNΦ. Immunofluorescent images representing the vasculature (vWF) in R53 glioma tumors in anti-LY6G Ab or isotype control treated mice, depletion 10 days after tumor induction (A) and after 4 weeks (B) Scale bar = 100µm. Quantification of blood vessels/ FOV, n=3. Mean ± SEM, unpaired Student t-test. p value of <0.05 was considered significant, (*) p<0.05, (**) p<0.01, (***) p<0.001. (C) RT-qPCR analysis of mRNA levels in BM-derived nNΦ and eNΦ for angiogenic markers. Gene expression was normalized to cyclophilin expression levels. Mean ± SEM. p value of <0.05 was considered significant, (*) p<0.05, (**) p<0.01, (***) p<0.001.

Table S1 related to STAR Methods. Mouse RT-qPCR primer list

Genes	Forward	Reverse
Acta	5’ GGACGTACAACTGGTATTGTGC 3’	5’ CGGCAGTAGTCACGAAGGAAT 3’
Arg1	5’ CTCCAAGCCAAAAGTCCTTAGAG 3’	5’ AGGAGCTGTCATTAGGGACATC 3’
CCL3	5' GATCTGGTTTCTCTTAGTC 3'	5' GAAGATTCCACGCCAATTCATC 3'
CCR2	5' ATCCACGGCATACTATCAACATC 3'	5' CAAGGCTCACCATCATCGTAG 3'
CCnd2	5’ GAGTGGGAACTGGTAGTGTTG 3’	5’ CGCACAGAGCGATGAAGGT 3’
CD34	5' AAGGCTGGGTGAAGACCCTTA 3'	5' TGAATGGCCGTTTCTGGAAGT 3'
Chi3l1	5’ GTACAAGCTGGTCTGCTACTTC 3’	5’ ATGTGCTAAGCATGTTGTCGC 3’
Ctgf	5’ GGGCCTCTTCTGCGATTTC 3’	5’ ATCCAGGCAAGTGCATTGGTA 3’
CXCL1	5' GCTGGGATTCACCTCAAGAA 3'	5' TGGCTATGACTTCGGTTTGG 3'
CXCL2	5' CCTGCCAAGGGTTGACTT 3'	5' CCTTGAGAGTGGCTATGACTTC 3'
Cyclophilin	5' CTGTGAGAG AACACCCAA AACA 3'	5' TTTGAACCATGAAGCCCTTGAT 3'
DDL3	5' CTGGTGTCTTCGAGCTACAAA T 3'	5' TGCTCCGTATAGACCGGGAC 3'
Fn1	5’ GCAGTGACCACCATTCCTG 3’	5’ GGTAGCCAGTGAGCTGAACAC 3’
G-CSF	5' GCAGGCTCTATCGGGTATTTC 3'	5' AGATGGTGGTGGCAAAGTT 3'
HHEX	5’ CGGACGGTGAACGACTACAC 3’	5’ CGTTGGAGAACCTCACTTGAC 3’
ICAM1	5' CTGTTTGAGCTGAGCGAGAT 3'	5' AACGAATACACGGTGATGGTAG 3'
IL-β	5' CCACCTCAATGGACAGAATATCA 3'	5' CCCAAGGCCACAGGTATTT 3'
iNOS	5’ GTTCTCAGCCCAAACAATACAAGA 3’	5’ GTGGACGGGTCGATGTCAC 3’
Itgb1	5’ TGTGGGCAACACTTTGACCC 3’	5’ CACAGTACAGCCCTTGATGTTTA 3’
MMP9	5’ TGAGTTCCAGGGCACACCA 3’	5’ TGTCTGGAGATTCGACTTGAAGTC 3’
NCAM	5' ACCACCGTCACCACTAACTCT 3'	5' TGGGGCAATACTGGAGGTCA 3'
NKX2-2	5' -AAG CAT TTC AAA ACC GAC GGA 3'	5' CCT CAA ATC CAC AGA TGA CCA GA 3'
Olig2	5' TCCCCAGAACCCGATCTT 3'	5' CGTGGACGAGGACACAGTC 3'
Osmr	5’-CATCCCGAACGAAAGTCTTGG-3’	5’-GGCTGGGACAGTCCATTCTAAA-3’
PARP1	5'TCATCTACGGCAACTGCAAGT 3'	5' AGCTCAGTATATGTGAGGTGGTC 3'
Stat3	5’ TGGCACCTTGGATTGAGAGTC 3’	5’ GCAGGAATCGGCTATATTGCT 3’
VEGFα	5' AAAGGCTTCAGTGTGGTCTG 3'	5' GGTTGGAACCGGCATCT 3'